

3 Main Linac

3.1 Introduction

In this chapter, we describe the layout and the properties of the main linacs, in which the electron and positron beams are accelerated from 5 to 250 GeV at a gradient of $E_{acc}=23.4$ MV/m. The electron and positron linacs have a total length of 14.4 km each, including a $\sim 2\%$ overhead for energy management in case of klystron failures. The 10,296 9-cell cavities per linac are contained in cryomodules (12 cavities per module, see section 3.2.4), which also house the focusing quadrupoles, steering magnets, and beam position monitors (BPM).

The radio frequency (RF) system (section 3.3) consists of 286 10 MW klystrons per linac (including overhead), which are installed in the tunnel and connected to the pulsed power supplies (modulators) in the external service halls by high voltage cables. The linac is operated at a pulse rate of 5 Hz, except for the first 3 km of the electron linac where the pulse rate is doubled to accelerate both the collider beam and the beam driving the X-ray Free Electron Laser (chapter 9). The flexibility of the RF control system allows independent adjustment of the accelerating gradient for the alternating collider and FEL beam pulses.

The small design emittance requires careful control of the beam dynamics in the linac. This important issue is discussed in the following section.

3.2 Beam Dynamics

To achieve the desired high luminosity, long trains of bunches with small transverse emittances are required. In this section, emittance preservation during acceleration in the main linac is discussed. The primary sources of transverse emittance dilution in a high energy linear accelerator are the transverse wakefields excited in the accelerating sections in the presence of imperfections, and the dispersive errors caused by the focusing magnets. For TESLA, the low RF frequency and corresponding large irises of the accelerating structures result in much smaller wakefield kicks for a given misalignment than in higher frequency room-temperature designs. Furthermore, a given dispersion generates less emittance blow-up, because the beam energy spread is kept small along most of the accelerator. The small wakefields and low energy spread ultimately result in relatively relaxed alignment tolerances for the various components (focusing magnets, beam position monitors, accelerating structures), for which modern optical survey techniques in combination with the standard beam-based alignment

	Collider	FEL
Accelerating gradient E_{acc} [MV/m]	23.4	9.2–23
Injection energy E_i [GeV]	5	2.5
Bunch charge N_e [10^{10}]	2.0	0.63
Bunch spacing Δt_b [ns]	337	93
Bunch length σ_z [μm]	300	25–50
Norm. design emittance ϵ_x, ϵ_y [10^{-6}m]	10, 0.03 (at IP)	1.5 (at undulator)
Norm. emittance at injection ϵ_x, ϵ_y [10^{-6}m]	8, 0.02	0.9
Beam size at injection $\sigma_{x,i}, \sigma_{y,i}$ [μm]	320, 16	150
Beam size at linac exit $\sigma_{x,f}, \sigma_{y,f}$ [μm]	60, 3	$\approx 35\text{--}60$
Initial uncorr. energy spread $\sigma_{E,i}/E$ [%]	2.5	0.1
Off-crest RF phase Φ_{RF} [$^\circ$]	5	0–30
Correlated energy spread δ_{cor} [10^{-4}]	3	10–1
Total spread $\sigma_{E,f}/E$ at linac exit [10^{-4}]	6	10–1.5

Table 3.2.1: Overview of beam parameters in the main linac.

procedures are sufficient. Table 3.2.1 lists all important linac parameters relevant to beam dynamics issues for both the HEP and FEL beams.

3.2.1 Beam optics

The beam is kept focused in the linac by means of a FODO lattice, which is characterised by its phase advance and beta functions. The wakefields are sufficiently small that suppression techniques such as Balakin-Novokhatski-Smirnov (BNS) damping [1] are not required, and a relatively large beta function and a weak beta scaling with energy can be used. The wakefield effects are dominant for large beta values (less quadrupoles) whereas the chromatic effects are dominant for small beta values (more quadrupoles). The TESLA lattice represents an optimised solution which balances the two contributions to the transverse emittance growth. The linac is divided into two sections:

- from 5 to 125 GeV, a FODO cell with $\beta_{max} = 127$ m and a cell length of 65 m is used, which is constructed from four accelerator modules;
- from 125 to 250 GeV, a longer cell (96 m) with $\beta_{max} = 167$ m is used, constructed from six modules.

The phase advance per cell is 60° in both cases. There are 365 FODO cells in total, so that the phase advance over the entire linac is about $60 \times 2\pi$. The maximum required quadrupole field at 400 GeV is 47 T/m for a magnetic length of 0.6 m. For orbit correction, every quadrupole contains a vertical correction coil, with an additional horizontal coil for every second (horizontally focusing) quadrupole. The vertical coils are also used to provide the small deflection required to follow the curvature of the earth, for

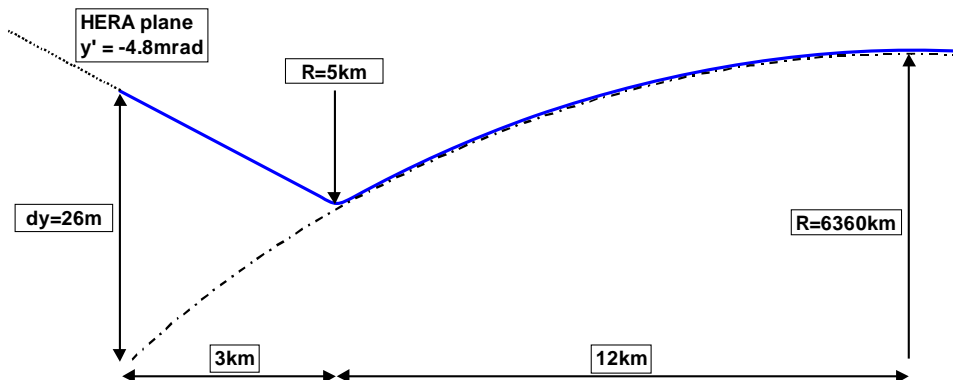


Figure 3.2.1: Vertical profile of the beam orbit (blue line) in the electron linac.

which a maximum integrated field gradient of 0.01 Tm is required (at 400 GeV). The effect of synchrotron radiation emitted in the steering magnets on the beam emittance and energy spread is negligible.

In the first 3km section of the electron linac, the 60° -lattice is also suitable for the FEL beam over most of its foreseen energy range. At low FEL energy operation (corresponding to an accelerating gradient of 9.2 MV/m, as compared to 23.4 MV/m for the High Energy Physics beam), a reduction to 45° per cell *for the high-energy beam* is necessary to avoid over-focusing of the lower-energy FEL beam, which sees a phase advance of 118° per cell (see also chapter 9). In addition, simultaneous operation of two very different energy beams in a linac which follows the curvature of the earth leads to intolerable systematic dispersive orbit offsets [2]. To avoid the latter effect, we have chosen to align this section of the linac along an exact straight line (in contrast to the previous layout [3]). Figure 3.2.1 shows the geometry. The beam line starts in the plane of the HERA ring, which is tilted with respect to the horizontal plane by an angle of -8 mrad. The transition to the line following the earth's curvature is provided by an achromatic bend insertion directly after the high-energy FEL beam extraction point. The emittance increase due to synchrotron radiation is negligible for the 50 GeV beam, and is still tolerable for the case of the linac-ring e-p collider option, where a beam of several hundred GeV would have to pass through this bending section in the opposite direction.

3.2.2 Single bunch effects

We consider first the short-range wakefield effects: as a bunch travels through the accelerating structures, wakefields are excited which act back on the bunch itself. The longitudinal wakefields affect the energy of the particles along the bunch, leading to a so-called correlated energy spread. For a beam which is off-axis in a cavity, the transverse wakefields tend to deflect the tail of the bunch away from the axis, resulting in a 'banana shape' of the bunch and a corresponding increase of the transverse emittance.

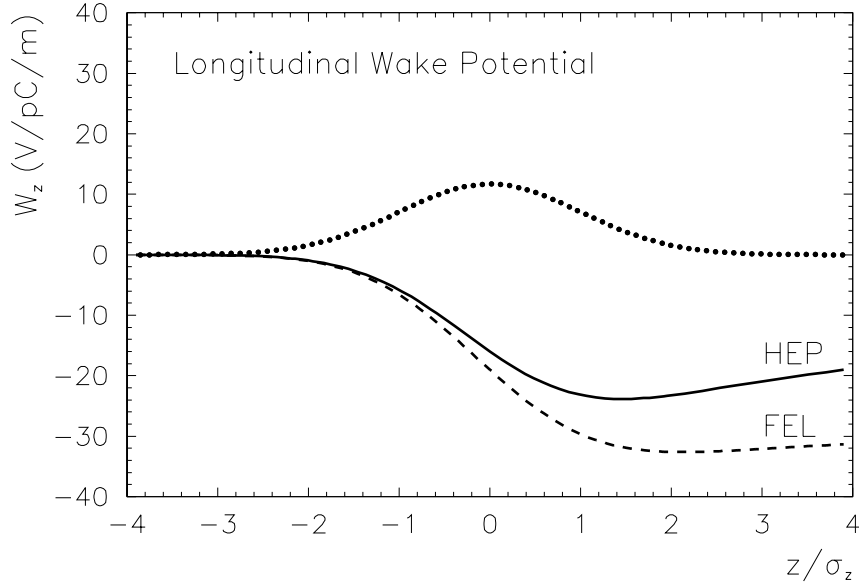


Figure 3.2.2: Longitudinal wake potential for $\sigma_z = 300\mu\text{m}$ (High energy Physics beam, HEP) and $\sigma_z = 25\mu\text{m}$ (Free Electron Laser beam, FEL). The dotted line indicates the charge distribution of the bunch.

3.2.2.1 Longitudinal single bunch dynamics

The longitudinal wakefields for the TESLA 9-cell cavities and a short bunch length ($\sigma_z < 1\text{ mm}$) have been carefully calculated. As the bunch travels through the cavities, the wakefield changes, and only reaches a steady state after passing through a number of structures. To correctly determine this steady state wake for the long periodic array of cavities in the linac, the computations were carried out for a chain of up to 16 cavities [5, 6]. From these calculations an analytic approximation for the point charge wake function per unit length of accelerating structure was derived:

$$w(s) = -38.1 \left[\frac{\text{V}}{\text{pC} \cdot \text{m}} \right] \left(1.165 \cdot \exp \left(-\sqrt{\frac{s}{3.65 \cdot 10^{-3} \text{ m}}} \right) - 0.165 \right).$$

The corresponding wake potentials for Gaussian bunches of length $\sigma_z = 300\mu\text{m}$ (HEP collider beam) and $\sigma_z = 25\mu\text{m}$ (FEL beam) are shown in figure 3.2.2.

The correlated energy spread induced by longitudinal wakefields can be minimised by running the bunch at the optimal RF-phase. This method works well for the 500 GeV collider parameters, but is less efficient for the FEL beam due to the short bunch (see figure 3.2.3 and table 3.2.1). In addition to the correlated energy spread induced by the wakefields and the curvature of the applied RF, there is an initial uncorrelated energy spread present in the injected beam (generated in the bunch compressor), which decreases adiabatically with acceleration. At injection, this energy spread is 2.5% and 0.1% for the collider and FEL beams respectively, and must be included in the

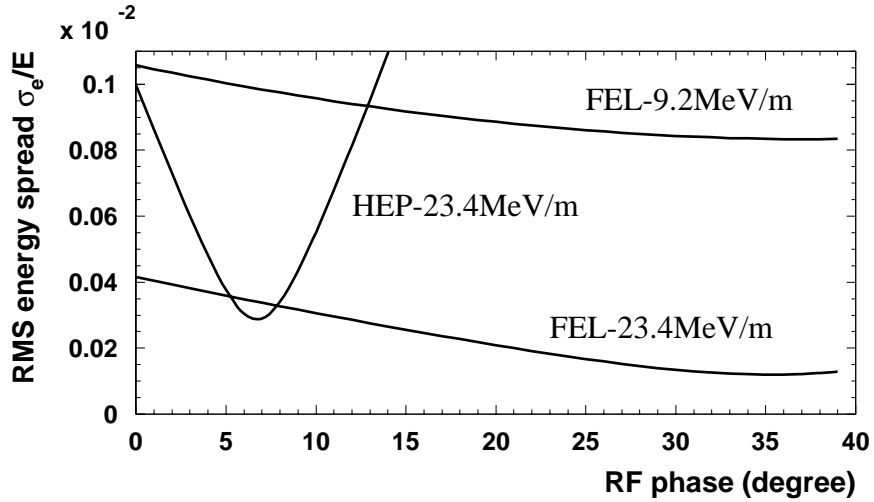


Figure 3.2.3: *Correlated rms energy spread as a function RF-phase for the High Energy Physics (HEP) ($E_{acc}=23$ MV/m) and Free Electron Laser (FEL) ($E_{acc} = 9.5-23$ MV/m) beams.*

calculations of chromatic emittance growth.

3.2.2.2 Transverse single bunch dynamics

For beam dynamics studies in the transverse plane, we need the transverse wake excited by a point-like charge (Green's function), while cavity codes only give the transverse bunch wake of a displaced bunch. The transverse impulse factor k_{\perp} (a quantity proportional to the total transverse momentum given to the bunch by its own wake) has been computed for different bunch lengths [4, 3]. A fit of k_{\perp} suggests a $\sigma_z^{1/2}$ dependence. The corresponding required delta wake per unit length is deduced from the fit of the transverse impulse factor:

$$W_{\perp}(s) = 1290 \sqrt{s/m} - 2600 s/m \quad (\text{V/pC/m}^2)$$

where s is the position *behind* ($s > 0$) the exciting point-like charge. When a bunch is injected off-axis, it performs a betatron oscillation about the central orbit. The tail particles of the bunch are then resonantly driven by the wakefield excited by the head particles. As a result, the amplitude of the oscillation grows rapidly as the beam travels down the linac. This effect leads to a tolerance on the allowed amplitude of the betatron oscillation. For the high-frequency machines, the wakefields are strong and the corresponding amplitude tolerance very tight, and BNS damping must be used to reduce the resonant effect. BNS damping works by making the head more energetic than the tail of the bunch, and the transverse wake effect is then partially compensated by the chromatic phase advance of the trailing particles. The disadvantage of BNS is the relatively large correlated energy spread that is required, which results in a

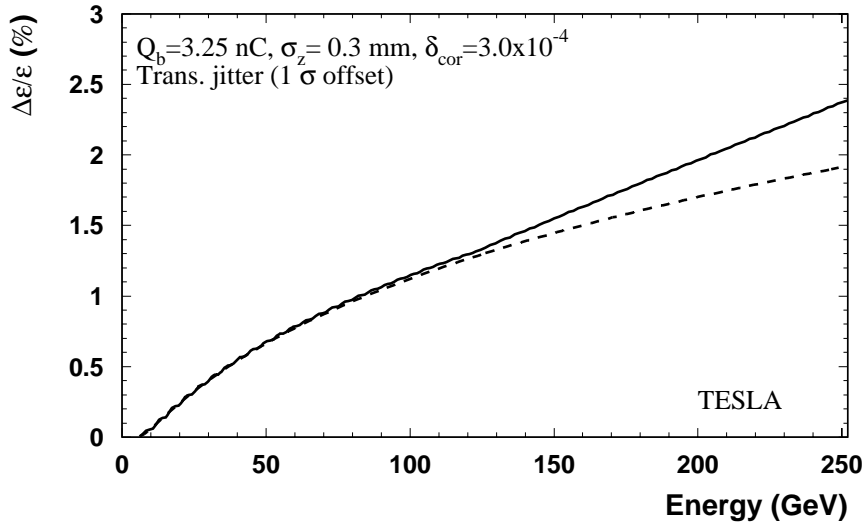


Figure 3.2.4: Vertical emittance growth from transverse wakefields with a beam offset equal to the rms vertical beam size. Full line: focusing lattice with β -step at half of linac length, dashed line: constant- β lattice.

larger dispersive emittance dilution due to quadrupole misalignments. Fortunately, BNS damping is not required for TESLA due to the weak wakefields, and the energy spread can then be kept at its minimum value along the entire linac. Figure 3.2.4 shows the development of the emittance growth along the linac for the linac lattice as described above, with an initial beam offset equal to a one rms beam size and no BNS damping. We note that even without BNS damping, the final emittance growth from the transverse wakefield is less than 2.5%. When the initial uncorrelated bunch energy spread is taken into account, an additional emittance dilution occurs due to chromatic filamentation. Performing the calculation again for one σ_y injection error yields $\Delta\epsilon_y/\epsilon_y=6\%$. For the FEL beam, the emittance growth is below 1%.

Next, we study the emittance growth caused by the transverse wakefields of randomly misaligned cavities. The average emittance dilution for the collider beam, calculated from 50 different random seeds of cavity misalignments with $\delta y_c=0.5$ mm (rms), is $\Delta\epsilon_y/\epsilon_y=7\%$ (see figure 3.2.5). The effect is negligible for the FEL beam. A further reduction of emittance growth is possible by using a non-dispersive orbit bump method: with only two closed bumps at different positions in the linac we obtain a residual emittance dilution at the end of the linac of $\Delta\epsilon_y/\epsilon_y \approx 1\%$. While it may be questionable whether the emittance can be measured with an accuracy of less than 1%, the bump method can still be useful for an empirical optimisation of the collider luminosity.

In order to avoid a continually growing trajectory in the presence of quadrupole alignment errors, the beam must be steered all along the linac. The simplest trajectory correction is the so-called ‘one-to-one’ method, where the dipole correctors steer the

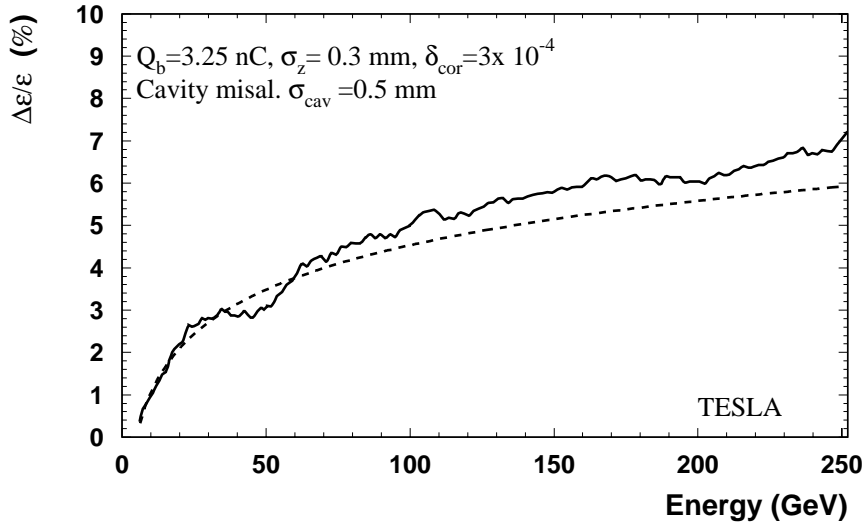


Figure 3.2.5: Vertical emittance growth obtained from computer simulation of 50 random seeds of cavity misalignments ($\delta y_c = 0.5$ mm rms). The dashed curve is the analytical prediction from a two-particle model.

beam to the magnetic centres of the quadrupoles using BPM measurements. Since the actual orbit will then follow the BPM misalignments, dispersive errors will arise. The realistic alignment errors after installation and survey of the linac modules are 0.3 mm (rms) for the quadrupoles and 0.1 mm (rms) for the BPMs with respect to the quadrupole centres. From simulations of the current lattice, the mean emittance growth due to the above random alignment errors — and after one-to-one steering — is one order of magnitude larger than the vertical design emittance. While this is acceptable for the initial commissioning of the machine, more elaborate correction algorithms are required for high luminosity operation:

- initial beam-based alignment techniques; and
- dispersion-free (DF) steering.

Beam-based alignment differs from the more standard optical alignment (survey) techniques in that the misalignments are deduced from BPM measurements with different beam trajectories. Beam-based alignment and correction has been developed and applied at the Stanford Linear Collider (SLC), the Final Focus Test Beam (FFTB), and several electron storage rings (for example see [7, 8, 9, 10, 11]), and can be considered a well established technique. The basic idea behind all the methods is to effectively replace the absolute error of an orbit measurement by the *relative* error of the BPM (i.e. its resolution), which is much smaller than the absolute BPM misalignment. For example, in the ‘shunt’ technique the strength of a single quadrupole is changed and the variation of the orbit downstream is measured. If the beam is steered through the magnetic centre of the quadrupole, the difference orbit becomes zero. The BPM next

to the quadrupole then shows its relative offset with respect to the quadrupole centre, with a precision equal to the BPM resolution. In contrast to this local method, the dispersion free (DF) steering algorithm [12] uses the variation of the strength of all quadrupoles simultaneously in the entire linac or a sub-section of it. The applied correction algorithm aims at minimising the measured difference orbit and thus effectively eliminates the absolute BPM offsets. We have investigated both the shunt method and the DF algorithm and found that a BPM [13] resolution of $10\ \mu\text{m}$ (rms) is sufficient to limit the dispersive emittance growth in the linac to a few %. The results of computer simulations for the DF method are shown in figure 3.2.6. The dispersive emittance growth obtained by averaging over 50 random seeds of misalignments amounts to 1% for an iterative procedure, in which the DF-algorithm is applied to sections of 20 FODO cells per step (see [14] for details). The residual orbit deviations after DF-correction yield an additional emittance growth from the transverse wakefield of 2% (figure 3.2.6).

In addition to a transverse alignment error, the cavity can be tilted longitudinally. The accelerating field then gives an additional transverse kick to the beam, with a strength which depends on the longitudinal position in the bunch. The tolerance on the cavity angle error has been estimated from numerical simulations at 0.5 mrad.

3.2.3 Multi-bunch effects

The TESLA beam pulse is composed of many bunches. Each bunch feels the accumulated effects of the long-range wakefields of all the preceding bunches. As a result, the amplitude of oscillation of the bunches increases rapidly as the bunch train travels down the linac. This phenomenon, called multi-bunch beam breakup (BBU), sets the tolerance on the cavity alignment with respect to the beam axis. In addition the bunch-to-bunch energy deviation will introduce a multi-bunch emittance growth, analogous to the single bunch dispersive dilution already mentioned.

3.2.3.1 Longitudinal multi-bunch dynamics

The inter-bunch energy spread should be smaller than the single-bunch energy spread in order to avoid strong additional chromatic effects. The multi-bunch energy spread is mainly produced by the transient beam loading in the accelerating structures. Fortunately, the high beam loading will be compensated in the standing-wave TESLA cavities by matching the power extracted by the beam to the RF power supplied by the klystron. A residual energy gain variation along the beam pulse is mainly caused by Lorentz force detuning and microphonics in the cavities, and RF mismatches; these will be suppressed by a feedback system down to $5 \cdot 10^{-4}$. The dispersive orbit variation over the bunch train is then of the order of a few tenths of the vertical beam size (rms). This does not present a problem in the linac and, since the energy variation takes place on a time scale much longer than the bunch spacing, it will be removed by the fast orbit correction feedback in the beam delivery system (chapter 7).

Because of the natural frequency spread of the longitudinal higher-order modes

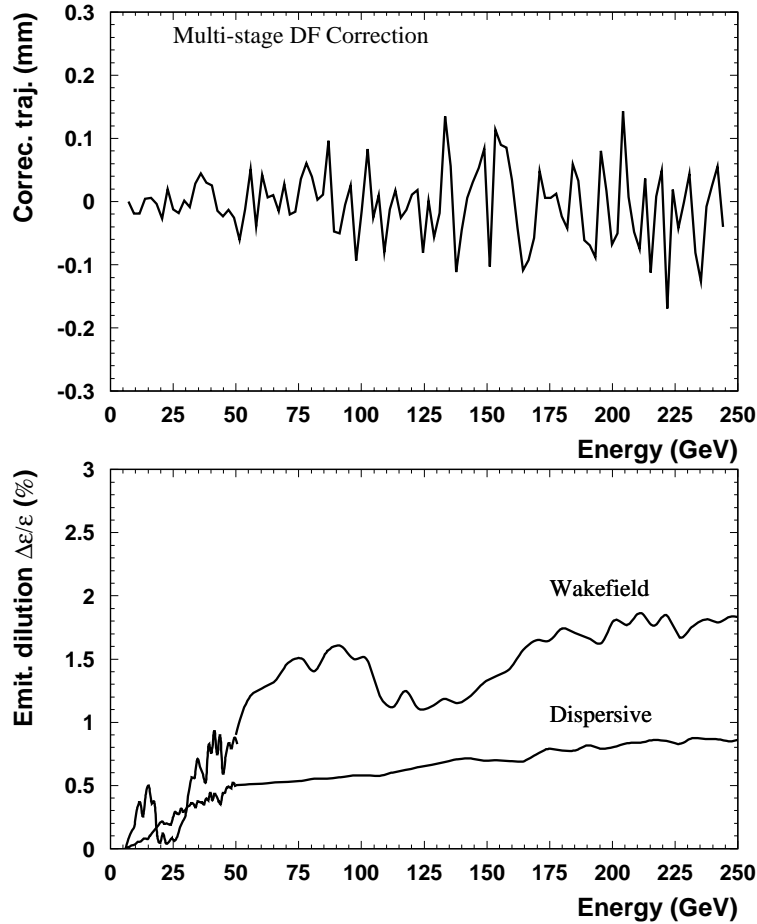


Figure 3.2.6: *Beam orbit (upper figure) and emittance growth (lower figure) after multi-stage dispersion free correction.*

(HOM), the resulting energy kicks given to the bunches of the train cancel out, and the total effect is therefore negligible.

3.2.3.2 Transverse multi-bunch dynamics

With a train of bunches, the long-range wakefields excited by each bunch will act on the subsequent bunches. The major effect comes from the multi-bunch beam break-up (or cumulative BBU) instability. Two methods are used to suppress the effects of cumulative BBU: cavity detuning and damping. The required random detuning of the transverse HOMs is naturally provided by cavity fabrication errors. As long as the bunch displacements are small, the effective wake is the average of the individual modes over many structures. For a Gaussian distribution of errors (HOM frequencies) and an infinite number of cavities, the effective wake would be reduced by the factor

$$\exp \left[-1/2(\sigma_{\omega}\tau)^2 \right],$$

Frequency (ave. meas.) [GHz]	Loss factor (simulation) [V/pC/m ²]	R/Q (simulation) [Ω/cm ²]	Q (meas.)
TE₁₁₁-like			
1.6506	19.98	0.76	7.0·10 ⁴
1.6991	301.86	11.21	5.0·10 ⁴
1.7252	423.41	15.51	2.0·10 ⁴
1.7545	59.86	2.16	2.0·10 ⁴
1.7831	49.20	1.75	7.5·10 ³
TM₁₁₀-like			
1.7949	21.70	0.77	1.0·10 ⁴
1.8342	13.28	0.46	5.0·10 ⁴
1.8509	11.26	0.39	2.5·10 ⁴
1.8643	191.56	6.54	5.0·10 ⁴
1.8731	255.71	8.69	7.0·10 ⁴
1.8795	50.80	1.72	1.0·10 ⁵
TE-like			
2.5630	42.41	1.05	1.0·10 ⁵
2.5704	20.05	0.50	1.0·10 ⁵
2.5751	961.28	23.80	5.0·10 ⁴

Table 3.2.2: *Dipole modes with highest loss factors of the 9-cell cavities as used for the multi-bunch beam dynamics simulations. The average frequencies and the Q values are taken from measurements at the first 3 TTF modules. The loss factors were obtained from MAFIA simulations.*

where σ_ω is the rms angular frequency spread and τ the elapsed time. In reality, the averaging is performed over a finite number of sections and the wake envelope does not vanish completely, but re-coheres at a later time: therefore, in order to reduce the effective wake for the rest of the long TESLA bunch train, a small damping is required. The lower the quality factor Q, the less will the excited field persist over the bunch train. The quality factors of the modes are reduced by means of HOM dampers, which are mounted at both ends of a TESLA cavity. The parameters of the dipole modes used for the multi-bunch calculations (frequency, geometric impedance and Q) are given in table 3.2.2. The assumed damping, with Q values of around or below 10⁵ for the highest R/Q modes, are in agreement with measurements made at the TTF. For a few of the cavities installed in the TTF linac, one dipole mode (at 2.58 GHz) has shown a Q value higher than assumed [15]: however, it is expected that by a better control of the mechanical tolerances of the cavities or a re-arrangement of the HOM-couplers (or both), this can be cured. We shall also see below that most of the BBU effect can be removed by the fast intra-train orbit correction system, so that it remains uncritical even in the case of a higher Q.

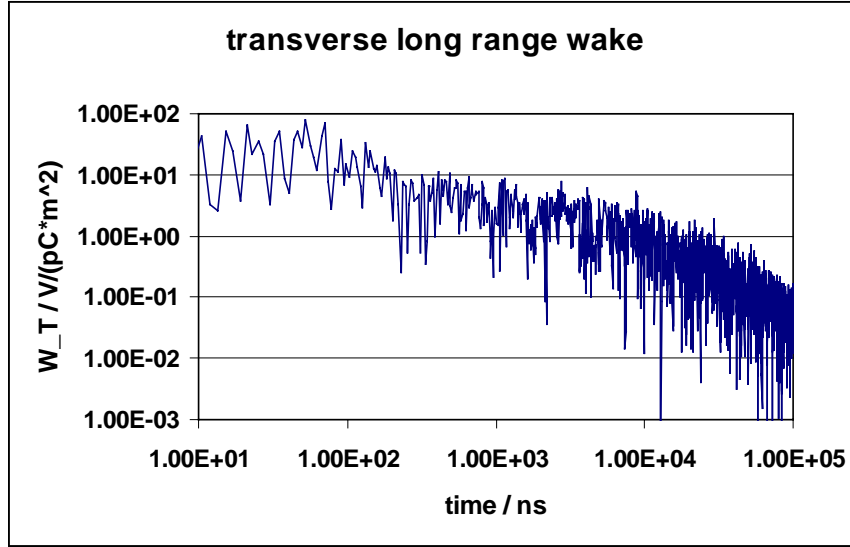


Figure 3.2.7: *Transverse long-range wake, calculated with the HOMs listed in table 3.2.2, and averaged over 36 cavities with a frequency spread of 0.1%.*

The effective dipole wake after detuning and damping is plotted in figure 3.2.7. After one bunch spacing (337 ns) the wake has decreased by an order of magnitude, and after about 100 μ s the HOM damping becomes effective. The multi-bunch emittance growth for the whole train has been obtained from computer simulations, and is shown in figure 3.2.8 (averaged over 10 different random seeds of cavity misalignment, with $\delta y_c = 0.5$ mm rms, no quadrupole misalignments). The mean value of the relative multi-bunch emittance growth is only 3%. The corresponding rms bunch orbit offsets are about two tenths of the beam size, sufficiently small to avoid an additional contribution to the single bunch emittance growth.

One of the advantages of the long TESLA pulse is that even with weak damping, a ‘steady state’ of HOM excitation is reached after a small fraction ($\sim 10\%$) of the bunch train. This can be seen in figure 3.2.9, where the individual orbit offsets of the bunches at the end of the linac are shown. Since only the fluctuation of the bunch offsets (and angles) around the average orbit matters for the emittance dilution, the rapid transition to a steady state helps to limit the BBU-driven emittance dilution to a tolerable value. We should point out that even a less favourable situation (e.g. when some of the HOMs have higher Q-values than expected, or the machine is operated with shorter pulses) does not present a serious problem regarding the multi-bunch dynamics, since the pattern of bunch offsets is essentially static, i.e. reproducible from pulse to pulse. It can therefore be removed by the fast orbit correction system after the linac, operating in a feed-forward mode. We have investigated with computer simulations the stability of the bunch orbit offsets with respect to the average orbit under the influence of ground motion, injection errors and bunch-to-bunch charge fluctuation [17]. One

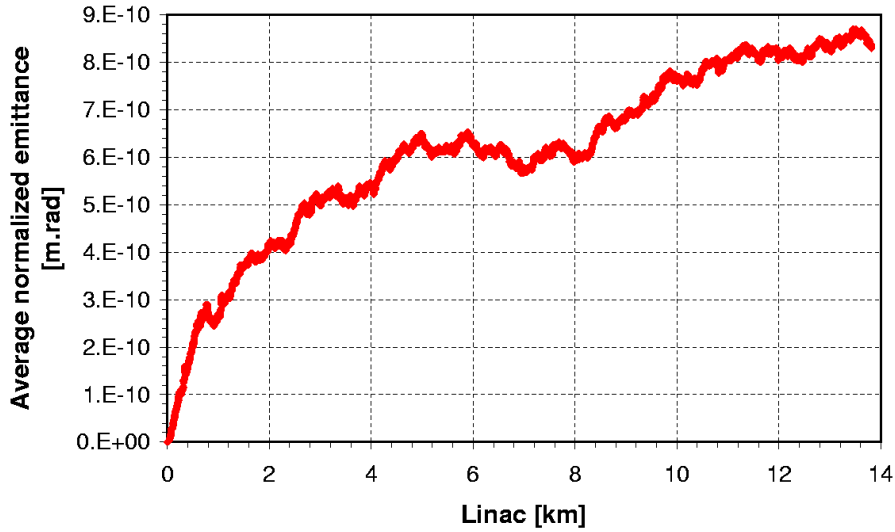


Figure 3.2.8: *Multi-bunch emittance growth along the linac, averaged over 10 random seeds of cavity misalignments ($\delta y_c = 500 \mu\text{m}$).*

such simulation result is shown in figure 3.2.9 for the example of a one σ_y injection error. The entire bunch train at the end of the linac is shifted because of the coherent betatron oscillation, but the pattern of orbit offsets due to HOMS remains almost unchanged: after subtracting the average orbit difference, the change in the individual bunch offsets is less than $10^{-2}\sigma_y$ rms from all of the above mentioned effects.

3.2.3.3 Orbit stability

Ground motion is of major concern because it will over time displace the quadrupoles, which in turn will dilute the beam emittance in the linac through dispersive effects. Numerous power spectra of ground motion have been measured at different sites. At low frequency, the motion can be quite large and is usually described by the ‘ATL’ rule, which states that the relative rms displacement Δy of two points separated by a distance L and after a time T (A is a constant which depends on the geology of the considered site) is given by

$$\Delta y^2 = A \cdot T \cdot L.$$

Slow orbit correction (feedback) can be used up to a frequency of some small fraction of the repetition rate (=5 Hz). At higher frequencies, the ground motion (vibration) amplitude falls off rapidly, but occurs too fast to use beam orbit feedback with simple steering magnets.

We have derived realistic estimates of orbit stability in the TESLA linac from ground and orbit motion measurements in the HERA storage ring (see for example [18, 19]). From these data, we can characterise the high frequency regime by an uncorrelated

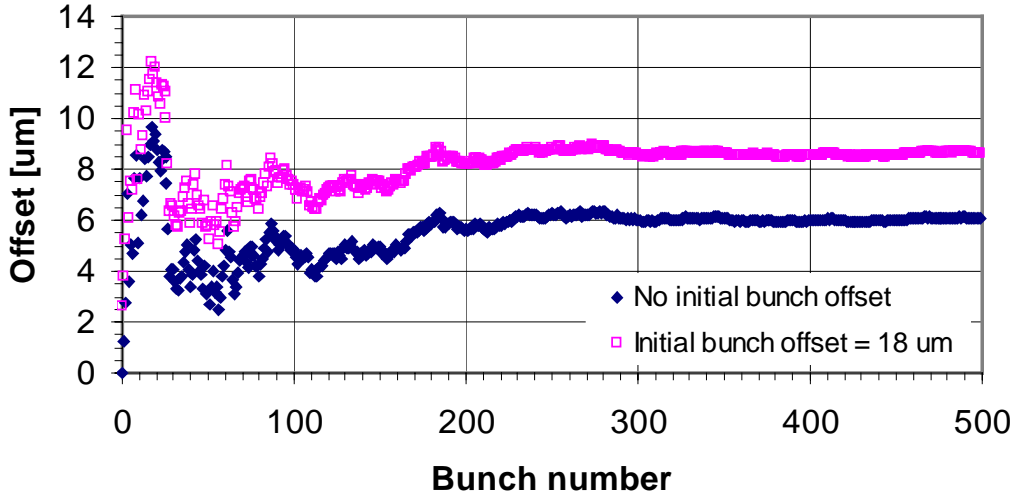


Figure 3.2.9: Orbit offsets in μm of the first 500 bunches at the end of the linac. The lower curve shows the effects of cavity misalignments only ($\Delta y_c = 0.5 \text{ mm rms}$, one seed). The upper curve shows the effects of the same misalignments, but with an additional one σ_y injection error of the beam (coherent betatron oscillation).

quadrupole vibration with an rms amplitude of $\Delta y_Q = 50\text{--}100 \text{ nm}$. This causes an orbit jitter Δy_{rms} at the end of the linac of

$$\Delta y_{rms} \approx 0.03 \mu\text{m} \cdot \frac{\Delta y_Q}{\text{nm}}, \quad (3.2.1)$$

corresponding to 0.5–1 times the beam size $\sigma_{y,f}$. This jitter does not present a problem for the beam dynamics in the linac itself, but it has to be corrected by the fast intra-train orbit feedback system in the beam delivery system in order to keep the beams in collision with the required accuracy (see chapter 7). On a longer time scale, slow diffusive ground motion (ATL) becomes the dominant effect. From the HERA data we obtain $A \approx 4 \cdot 10^{-6} \mu\text{m}^2/\text{s/m}$. The calculated orbit drift at the end of the linac is then

$$\Delta y_{rms} \approx \sigma_{y,f} \cdot \sqrt{t/30\text{s}}.$$

This drift is sufficiently slow to be able to use steering magnets for maintaining the beam on the ‘golden’ orbit, previously established by beam-based alignment and DF steering. After a longer time, when the position drift of the quadrupoles (and BPMs) becomes comparable to the BPM resolution, additional dispersive emittance growth is generated and the beam-based alignment has to be repeated. With the above assumption on diffusive ground motion, the dispersion free steering algorithm has to be applied on average about once per month.

3.2.4 Concluding remarks

The beam dynamics studies in the main linac have shown that with realistic assumptions on the alignment accuracy and orbit diagnostics precision, the small vertical beam emittance can be preserved. We expect a total emittance growth with respect to the design value at the IP of about 10%, which is well within the emittance growth budget of a factor of 1.5 between the damping ring and the IP. However, one has to be careful with the interpretation of the emittance dilution obtained here. The single bunch transverse wakefield kicks and dispersive effects from the longitudinal wakefield have not ‘filamented’ at the end of the linac, i.e. there remains a longitudinal-transverse correlation (‘banana effect’). In the regime of high disruption parameter, the beam-beam interaction tends to amplify such correlated distortions in the bunches and the resulting luminosity reduction can be larger than naively estimated by using the *projected* emittance to determine the effective beam size at the IP. This question is in more detail discussed in chapter 7.

section Accelerator Modules (Cryomodules)

The design of the so-called cryomodules has been primarily driven by the need to reduce costs compared to existing superconducting cavity systems. The module described here is based on the 3rd cryomodule generation of the TESLA Test Facility [20, 21]. Except for the length (≈ 17 m compared to 12 m for a TTF module), only minor modifications to the design have been made.

Present day superconducting cavity systems tend to have many separate cryogenic supply boxes and associated warm-to-cold transitions, which represent a significant fraction of the cost. The concept adopted here is to significantly reduce this number by having a single long continuous string of about 2.5 km — called a cryogenic unit — which is connected to one cryogenic supply box at the beginning and one end box. Long modules will be built consisting of twelve 9-cell cavities, a quadrupole, steering coils and a beam position monitor (BPM); the helium distribution system needed to operate the superconducting cavities and magnets at 2 K is also integrated into the module. The modules are then connected together to form a cryogenic unit.

3.2.5 The Cryostat

Figure 3.2.10 shows a longitudinal view of a cryomodule. The 300 mm diameter helium gas return pipe (GRP) is the main support structure for the string of cavities and magnets. The GRP is supported from above by three posts which provide the necessary thermal insulation to room temperature. The posts are fastened to large flanges on the upper part of the vacuum vessel by adjustable suspension brackets, allowing the axis of the cavities and quadrupoles to be correctly aligned, independent of the flange position.

The support system is designed to allow the GRP to contract/expand longitudinally with respect to the vacuum vessel during thermal cycling. The centre post is fixed to the vacuum vessel, while the two end brackets can move in the axial (z) direction to accommodate differential shrinkage. A post consists of a fiberglass pipe terminated by

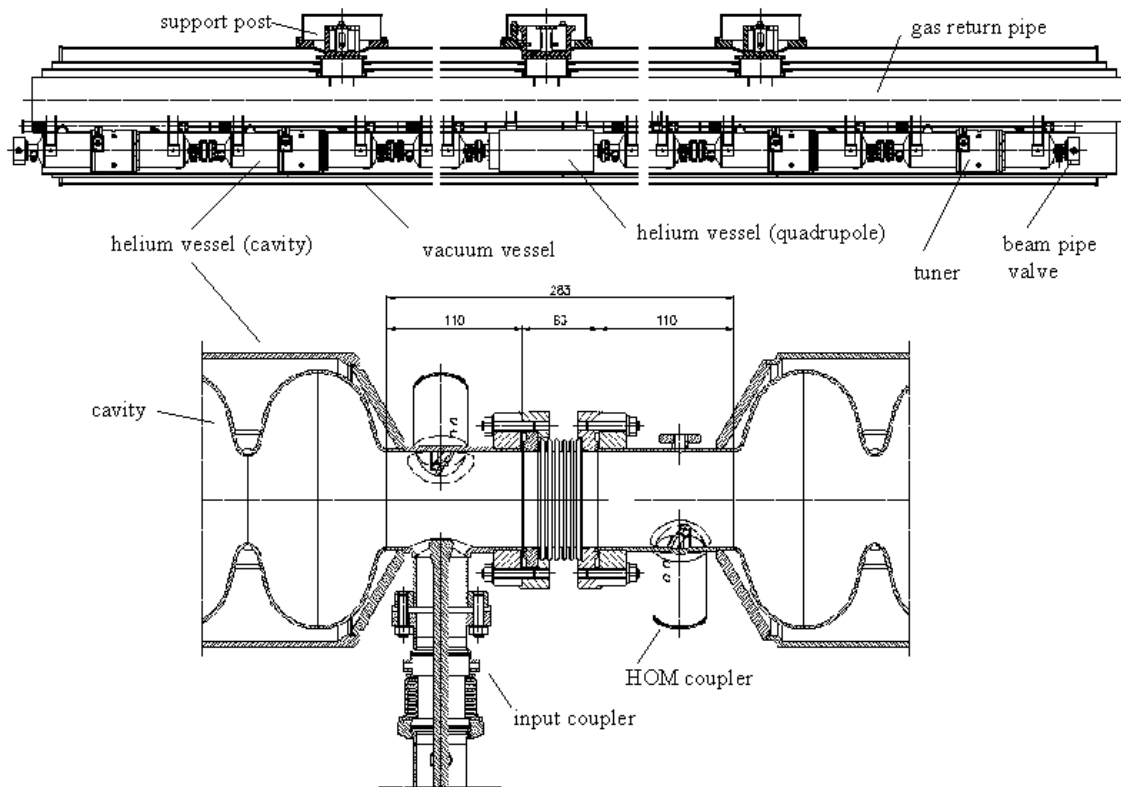


Figure 3.2.10: *Longitudinal view of a cryomodule.*

two shrink-fit stainless steel flanges. Two additional shrink-fit aluminum flanges are provided to allow intermediate heat flow intercept connections to the 5–8 K and 40–80 K thermal shields; the exact location of these flanges has been optimised to minimise the heat leakage. In addition, the post diameter has been optimised to prevent possible excitation of mechanical eigenfrequencies.

Each of the 12 cavities is encased in a titanium helium vessel, attached to the GRP by means of stainless steel brackets connected to four titanium pads on the vessel itself; each bracket is equipped with a longitudinal sliding mechanism and adjusting screws and pushers for alignment. A mechanical and a piezo-electric tuner are mounted to the vessel [22]. The inter-cavity spacing — which accommodates RF- and HOM-couplers and a flanged bellows — amounts to 283 mm.

Manually operated valves required by the clean-room assembly terminate the beam pipe at both module ends. The valves are fitted with simple RF shields [23].

During cool down the two ends of the ~ 17 m long gas return pipe move by up to 26 mm toward the centre of the module. To keep the cold input coupler head of each cavity fixed longitudinally within an accuracy of 1 mm, each cavity is anchored to a long invar rod attached to the longitudinal centre of the gas return pipe.

The beam pipe interconnection between the cryomodules consists of a 0.38 m long section that incorporates a Higher Order Mode (HOM) absorber, a bellows, and a

vacuum pumping port; the latter will be connected to a flange in the vacuum vessel every ninth cryomodule.

The cryostat includes two aluminum radiation shields operating in the temperature range of 5–8 K and 40–80 K respectively. Each shield is constructed from a stiff upper part (divided into two halves), and 12 (or 13) lower sections (according to the number of the cold active components, e.g. cavities, magnets). The upper parts are supported by the intermediate flanges on the fiberglass posts; they are screwed to the centre post but can axially slide on the other two posts, to which they are still thermally connected. The new ‘finger welding’ technique — successfully demonstrated at TTF — is used both to connect each thermal shield to its properly shaped aluminum cooling pipe, and the lower shield parts to the upper ones.

Blankets of multi-layer insulation (MLI) are placed on the outside of the 5–8 K and the 40–80 K shields. The 5–8 K shield blanket is made of 10 layers while the 40–80 K blanket contains 30 layers. In addition the cavity and quadrupole helium vessels, gas return pipe and 5–8 K pipes are wrapped with 5 layers of MLI to reduce heat transfer in the event of a vacuum failure.

Figure 3.2.11 shows a cross section of the cryomodule. The cryostat outer vacuum vessel is constructed from carbon steel and has a standard diameter of 38". Adjacent vacuum vessels are connected to each other by means of a cylindrical sleeve with a bellows, which is welded to the vessels during installation. Radiation shield bridges are also provided. In the event of accidental spills of liquid helium from the cavity vessels, a relief valve on the sleeve together with venting holes on the shields prevent excessive pressure build-up in the vacuum vessel. Wires and cables of each module are extracted from the module using metallic sealed flanges with vacuum tight connectors. The insulating vacuum system will be pumped during normal operation by permanent pump stations located every 250 m. Additional pumping ports are located every 50 m for movable pump stations, which are used for initial pump down, and in the case of a helium leak. The RF power coupler needs an additional vacuum system on its room temperature side; this is provided by a common pump line for all 12 couplers per module, equipped with an ion getter and a titanium sublimation pump.

The following helium lines are integrated into the cryomodules:

- The 2 K forward line transfers pressurised single phase helium through the cryomodule to the end of the cryogenic unit.
- The 2 K two phase supply line (made from titanium) is connected to the cavity and magnet helium vessels. It supplies the cavities and the magnet package with liquid helium and returns cold gas to the 300 mm GRP at each module interconnection.
- The 2 K GRP returns the cold gas pumped off the saturated He II baths to the refrigeration plant. It is also a key structural component of the cryomodule (see above text and section 3.2.7).
- The 5–8 K forward and return lines. The 5 K forward line is used to transfer the He gas to the end of the cryogenic unit. The 5–8 K return line directly cools the

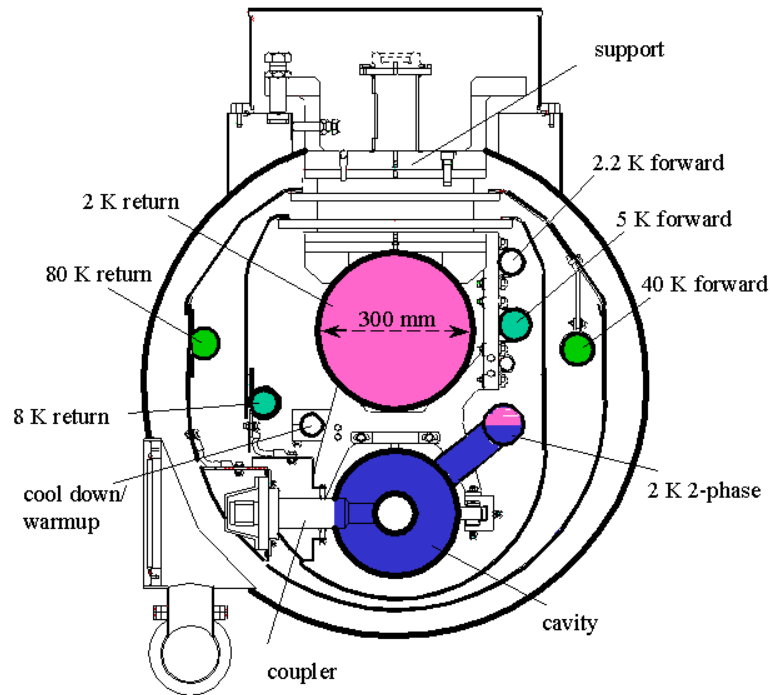


Figure 3.2.11: Cross section of cryomodule.

5–8 K radiation shield and, through the shield, provides the heat flow intercept for the main coupler and diagnostic cables, and the higher-order mode (HOM) absorber located in the module interconnection region.

- The 40–80 K forward and return lines. The 40 K forward line is used to transfer He gas to the cryogenic unit end and cools the high temperature superconductor (HTS) current leads for the quadrupole and correction magnets. The 40–80 K return line directly cools the 40–80 K radiation shield and the HOM absorber and, through the shield, provides an additional heat flow intercept for the main coupler and diagnostic cables.
- The warm-up/cool-down line connects to the bottom of each cavity and magnet helium vessel. It is used during the cool down and warm up of the cryostat.

The helium lines connected to the cavities and the magnets withstand a pressure of 4 bar; all other cryogenic lines withstand a pressure of 20 bar. The helium lines of adjacent modules are connected by welding, as was done for the HERA superconducting

magnets. Transition joints (similar to those used in the HERA magnets) are used for the aluminum to stainless steel transition on the thermal shield cooling lines.

The cryostat maintains the cavities and magnets at their operating temperature of 2 K. A low static heat load is an essential feature of the cryostat design; the total heat load is dominated by the RF losses, and is thus principally determined by cavity performance. Table 3.2.3 shows the calculated heat load for a cryomodule with cavities operating at the nominal accelerating gradient of 23.4 MV/m (21.1 MV/m is assumed as the maximum gradient for the FEL operation).

The short bunches in TESLA excite wake fields in a very wide frequency range which will be absorbed in the structure walls and therefore contribute to the cryogenic losses. Table 3.2.4 shows the single bunch losses calculated from the monopole short range wake [5, 6]. The effect of losses in a frequency range beyond the threshold for Cooper pair breakup (about 750 GHz) in superconducting niobium has been investigated in [24]: in a quasi-periodic string of 9-cell cavities the temperature rise of the inner cavity surface and the resulting Q_0 drop are negligible.

Most losses occur at lower frequencies where the conductivity of the superconducting surfaces is several orders higher than that of normal conducting walls. Part of this power is extracted by input- and HOM-couplers, but high frequency fields will propagate along the structure and be reflected at normal and superconducting surfaces [25]. In order to reduce the losses at normal conducting surfaces at 2 K and 4 K, a special HOM absorber is foreseen which operates at 70 K, where the cooling efficiency is much higher. The absorber basically consists of a pipe of absorbing material mounted in a cavity-like shielding, and integrated into the connection between two modules. As the inner surface area of this absorber (about 280 cm²) is small compared to that of all the normal conductors in one cryomodule, the absorber has to absorb a significant part of all the RF power incident upon it. In field propagation studies, which assume a gas-like behaviour for photons, it has been shown that an absorber with a reflectivity below 50% is sufficient [25]. Theoretical and experimental studies have suggested that the required absorption may be obtained with ceramics like MACOR [25, 26] or with artificial dielectrics [27].

The axes of the 12 cavities must be aligned to the ideal beam axis to within ± 0.5 mm, and quadrupole axes to within ± 0.2 mm. The quadrupoles have an additional ‘roll’ tolerance of ± 0.1 mrad.

The ambient magnetic field in the cavity region must not exceed $0.5 \mu\text{T}$ to preserve the low surface resistance. At TTF this has been achieved by demagnetising the vacuum vessel (made of soft steel) before assembly of the cryomodule, and placing a passive shield (made of Cryoperm) around each cavity helium vessel.

Several types of cryomodule are required in the machine:

- 1004 standard linac modules with 12 cavities and a length of 15.927 m;
- 742 standard linac modules with an additional quadrupole and corrector coil package (package length 0.864 m, which increases the module length by 0.801 m), are required every second module up to 125 GeV, and thereafter every third module;

	static [W]	dynamic [W], 23.4 MV/m, $Q_0 = 1 \cdot 10^{10}$, 5 Hz, high energy beam	add. dynamic [W], 21.1 MV/m, $Q_0 = 1 \cdot 10^{10}$, 5 Hz, FEL beam
2 K			
RF load	–	4.95	3.99
supports	0.60	–	–
input coupler	0.76	0.14	0.14
HOM coupler	0.01	0.27 ^{a)}	0.27 ^{a)}
HOM absorber	0.14	0.02	0.01
beam tube bellows (12)	–	0.24	0.20
HOM to structure	–	1.68	0.86
instrumentation cable	0.13	–	–
current leads	0.10	0.01	–
sum	1.74	7.31	5.47
5–8 K			
radiation	1.95	–	–
supports	2.40	–	–
input coupler	2.05	1.19	1.15
HOM coupler	0.40	2.66 ^{a)}	2.66 ^{a)}
HOM absorber	3.13	0.77	0.37
instrumentation cable	1.39	–	–
sum	11.32	4.62	4.18
40–80 K			
radiation	44.99	–	–
supports	6.00	–	–
input coupler	21.48	59.40	48.89
HOM coupler	2.55	13.22	13.22
HOM absorber	-3.27	15.27	8.07
instrumentation cable	5.38	–	–
current leads	13.00	5.00	–
sum	90.13	92.89	70.18

Table 3.2.3: Calculated heat loads for 17m long cryomodule with quadrupole. ^{a)} Worst case estimate, assuming resonant excitation of monopole modes.

	collider operation	FEL operation
total losses	23.3 W	14.2 W
losses above 10 GHz	12.7 W	9.4 W
losses above 750 GHz	< 0.001 W	0.5 W

Table 3.2.4: *Monopole single bunch losses in one cryomodule.*

- 27 cryomodules with 8 cavities and one quadrupole package are required for the FEL injector and the positron pre-accelerator; and
- 8 cryomodules with 4 cavities and 4 quadrupole packages are required for the positron pre-accelerator (see chapter 4).

In about every tenth cryomodule (the shortest cooling loop), three cryogenic valves (one JT-valve), three flow-meters and some instrumentation will be incorporated. This avoids extra string connection boxes which would require extra space (and cost).

3.2.6 Quadrupole and Correction Magnets

The quadrupole package is shown in figure 3.2.12. It consists of:

- a $\cos 2\Theta$ type quadrupole;
- correction dipoles for vertical and horizontal beam deflection;
- an iron yoke with shrink cylinder surrounding the magnet coils;
- a helium vessel;
- an RF beam position monitor (BPM);
- current leads.

To simplify the system, the quadrupole packages are cooled with 2 K super-fluid helium in the same manner as the cavities. Because of the small stored energy, the pressure in the 2-phase supply line will not increase beyond 3 bar during a quench. The magnet parameters are listed in table 3.2.5.

3.2.6.1 Quadrupoles

The linacs contain quadrupoles with a maximum gradient of 60 T/m (field integral 31.2 T). The quadrupoles are located at the centre of the cryomodules (generally underneath the central support post) to guarantee high positional accuracy. The operating current is limited to 100 A for cost reasons (minimum heat loads and low cost power supplies). The superconducting coils are of the $\cos 2\Theta$ type, wound in double layers from a flat ribbon made from electrically insulated superconducting wires. The coil has a large inductance (~ 3.2 H), and a quench must be detected fast so that an external dump resistor can be switched into the circuit for protection.

quadrupole coil ($\cos 2\Theta$, 2 layer)		
inner coil radius RQi	45	mm
outer coil radius RQo	66	mm
coil straight section length	520	mm
coil total length	626	mm
nominal gradient	60	T/m
max. field at conductor	3.6	T
operating temperature	2.0	K
nominal current	100	A
number of turns/pole	1007	
inductance	~ 3.2	H
dipole coils, vert./horiz. ($\cos\Theta$, single layer)		
inner coil radius RDi1	67	mm
outer coil radius RDo1	68	mm
inner coil radius RDi2 (in every 2 nd package)	69	mm
outer coil radius RDo2 (in every 2 nd package)	70	mm
coil straight section length	520	mm
coil total length	626	mm
max. field on axis	0.074	T
max. field at conductor	3.6	T
operating Temperature	2.0	K
max. current	40	A
number of turns(1)/pole	99	
number of turns(2)/pole	102	
inductance/coil	~ 29	mH
iron yoke		
inner yoke radius RYi	71	mm
outer yoke radius RYo	121	mm
yoke length	520	mm
helium vessel		
outer radius RVo	145	mm
inner beam pipe radius Rbi	39	mm
helium vessel length	666	mm
field quality (at $R_0 = 30$ mm)		
skew quadrupole (a_2)	$3 \cdot 10^{-4}$	
higher harmonics of quadrupole	10^{-3}	
alignment error (angle)	0.1	mrad rms

Table 3.2.5: Main parameters of the superconducting magnet package.

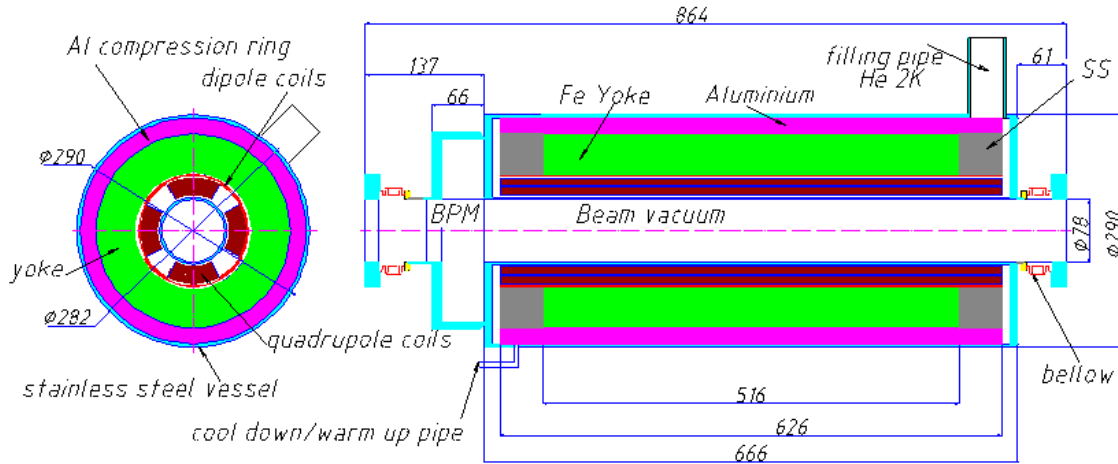


Figure 3.2.12: Cross-section and longitudinal cut of superconducting magnet package.

3.2.6.2 Correction dipoles

The correction dipoles have a maximum field of 0.074 T (field integral 0.038 Tm), which can correct a maximum beam offset (at $E_{beam} = 400$ GeV) of ± 3 mm per correction coil. There is one correction coil for vertical beam deflection in every magnet package and one for horizontal beam deflection in every second package. The coils are wound from a round multi-filament wire in a single layer on top of the quadrupole coils. The maximum dipole current is 40 A.

3.2.6.3 Iron yoke and shrink cylinder

The coil package is surrounded by a yoke made from 5 mm thick carbon steel laminations. At the coil ends the carbon steel is replaced by stainless steel. The laminations are held together by rods, and a shrink cylinder made from aluminum is placed around the yoke in order to apply the necessary force on the coils.

3.2.6.4 Helium vessel

The quadrupole, together with the correction dipole coils and associated yoke, are assembled in a helium vessel which consists of the electrically insulated beam pipe, the outer vessel, and the end plates of which one is part of the BPM. The beam pipe has bellows at both ends, and both the beam pipe and bellows are copper plated from inside. The outer vessel contains keys for proper alignment of the interior yoke and coils, and there are fiducial marks for alignment on the outside of the end plates. The end plates are covered with soft steel magnetic mirror plates to reduce the fringe fields.

3.2.6.5 Beam position monitor

The BPM is of the pill box type, and is attached to the end plate of the helium vessel. It is copper plated on the inside and equipped with two antennas for each transverse direction (x and y). The beam position measurement resolution is $10\ \mu\text{m}$ and the installation tolerance with respect to the quadrupole axis is 0.1 mm.

3.2.6.6 Current leads

The coils will be powered through current leads made from HTS in the low temperature region, and from normal conducting material in the upper part. For reasons of simplification and to avoid many valves in the tunnel, there is no gas cooling foreseen. The heat flow in the upper end of the HTS part is intercepted at 50 K from the 40–80 K forward line.

3.2.6.7 Quadrupole support and alignment

The quadrupole package is rigidly mounted to the 300 mm diameter GRP. The package is located underneath the centre post, which assures minimum motion during operation.

The relatively tight tolerances on the quadrupole field and BPM alignment have a major impact on their fabrication:

- the coils will be fabricated with high precision using precise tooling (radii and coil angles with tolerances of 0.02 mm);
- the yoke laminations will be fabricated by punching or fine blanking, assuring high accuracy;
- the helium vessel must be accurately fabricated and precisely assembled with the aid of pins, keys and reference targets at the end plates;
- the field axis and orientation will be accurately measured and referenced before and during installation;
- the BPM will be machined with high precision as an integral part of the helium vessel end plate.

In addition, the shrinking process during cool down leads to a tight fit between coils and yoke, which further assures the alignment.

3.2.7 Assembly and alignment

The design of the cryomodule — including fabrication procedures and tolerances — is the key factor to obtaining the required alignment precision for cavities and magnets, while at the same time limiting the costs. The final alignment of the individual active components is performed once the string of cavities is out of the clean room and anchored to the supporting GRP. The alignment of the GRP, via three Taylor-Hobson

spheres, is then used to reference the axis of the active components. Assembly and cool down do not affect this external reference, except for a predictable and reproducible parallel vertical motion.

A crucial step in cutting the production cost was to relax the general tolerances of the GRP and of the vacuum vessel, while using a long milling machine to precisely reference (after welding of ancillary components) all the important axes and planes. In particular, the GRP is now fabricated according to the standard tolerances for a high quality welded pipe (± 5 mm), including straightness. After welding of the cavity supports, lower post flanges and end flanges, the axis is defined on the milling machine according to the end flange centres and transferred to the lower post flanges. The interconnection bellows, properly fastened, are already included to minimize the inter-module lateral forces. The pipe is then turned and the cavity supports referenced to the defined GRP axis. A similar procedure is also applied to the vacuum vessel to reference the coupler ports and upper flanges to the vessel axis. After welding and before milling, a stress relief is performed on the GRP to avoid permanent deformation induced by thermal cycling.

The stretched wire measurements at TTF show that these procedures lead to the required accuracy.

The module assembly is performed in three major steps:

1. the cavity string is prepared in the class 10 clean room, pre-aligned and closed;
2. the string is then transferred to the assembly area where it is attached to the aligned GRP;
3. each cavity and quadrupole is aligned with respect to the GRP using the three optical targets on the posts (Taylor-Hobson spheres) and then fixed.

The module can now be moved and the alignment recovered through the external targets. The last step is performed in a third assembly station where, after the assembly of the thermal shields, a long fixed cantilever and a movable cart are used to insert the cold mass into the vacuum vessel. Module alignment in the linac is made using three optical targets placed on the vacuum vessel and referenced to those on the GRP.

3.3 RF System

3.3.1 Overview

The RF system consists of 286 stations per electron and positron main linac, each of which provides power at 1.3 GHz to a total of 36 accelerating cavities (three cryomodules, see section 3.2.4). The peak RF power needed for one superconducting cavity at full gradient and maximum beam current (23.4 MV/m and 9.5 mA) is 231 kW; the nominal peak power needed for 36 cavities is therefore 8.3 MW. Taking into account a regulation reserve of 10% for phase and amplitude control and another 6% for circulator and waveguide losses, a total of 9.7 MW is required. The RF pulse length is 1.37 ms, which includes the beam pulse length of 950 μ s, and the cavity fill time of 420 μ s. The repetition rate is 5 Hz for the major part of the linac: the 5–50 GeV section stations will run at 10 Hz to alternate between FEL and Linear Collider operation.

During the beam pulse the fluctuations of the accelerating field (defined as the vector sum of the fields in the 36 cavities) must be kept small. The major sources of field perturbations which have to be controlled by the low level RF system are fluctuations of the resonance frequency of the cavities and fluctuations of the beam current. Changes in resonant frequency result from deformations of the cavity walls induced by mechanical vibrations (microphonics) or the gradient dependent Lorentz force. Slow changes in frequency — on the time scale of minutes or longer — are corrected by a frequency tuner, while faster changes are counteracted by fast amplitude and phase modulation of the incident RF power.

The main components of the RF system are the modulators and klystrons. The modulator converts AC line power into high voltage pulse power; its main components are a high voltage power supply, a high voltage pulser unit and a pulse transformer. The klystron generates pulsed RF power from (pulsed) high voltage power, which is then distributed to the cavities by a system of waveguides. The circulators in the distribution system protect the klystron from reflected power. The low level RF system controls the shape, amplitude and phase of the RF. Various auxiliary devices for the klystron and modulator are also required. An interlock system protects the linac and the RF stations in case of malfunction.

In order to provide RF power for the entire linac at a centre of mass energy of 500 GeV, 560 RF stations are required. The number of installed systems will be 572 to provide an overhead for energy management in case of klystron failures. For the 800 GeV upgrade, the number of stations will be doubled to 1144. With the exception of the high voltage power supplies and pulser units for the modulators, the RF stations will be installed in the tunnel with a separation of 50 m (25 m for the 800 GeV). The high voltage power supplies and pulsers for the modulators will be installed in the access halls, which are separated by about 5 km. The connection between the pulser and pulse transformer will be accomplished by high voltage pulse power cables. There will also be additional cable connections for the interlock system between the halls and the tunnel. The number of modulators per hall will be typically 100.

In the remainder of this section, the various subsystems forming one RF station



Figure 3.3.1: *Cathode of the multibeam klystron.*

will be described.

3.3.2 High power RF source

Comparison of different types of klystrons constructed and built so far have shown that a low microperveance of the klystron electron beam ($p = 10^6 \times I/V^{3/2}$, where I and V are the klystron beam current and voltage respectively) results in a high efficiency [28, 29]. This is due to lower space charge forces in the beam, which make the bunching easier and more efficient. For a single beam klystron at very high output power, the demand for high efficiency leads to low microperveance and hence to very high voltage, resulting in a reduced reliability. The solution is to use a multibeam klystron, where many small low voltage, low microperveance beams are used in parallel in one vacuum vessel. With a multibeam klystron, an efficiency of 70% or more seems to be feasible, compared to a typical maximum of 45% for a 5 MW single beam klystron.

Figure 3.3.1 shows the cathode of the multibeam klystron constructed and built by Thomson Tubes Electroniques [30]. Seven beams are produced by the cathode and accelerated by the klystron gun. Each beam has a microperveance of 0.5. The beams share common cavities but have independent drift tube sections. After RF extraction in the output cavity, the spent electron beams are absorbed in the collector.

Figure 3.3.2 shows the complete TH1801 multibeam klystron (without solenoid). Two output waveguides are required to handle the RF power of 2×5 MW in the output



Figure 3.3.2: *The Thomson TH1801 multibeam klystron.*

windows. The total height of the klystron is 2.5 m. The klystron was successfully tested and is now in use at the TTF. It achieved an output power of 10 MW with an efficiency of 65%. Table 3.3.1 summarises the design parameters and the parameters achieved with the prototype tests. More detailed information can be found in [31].

The gain of 48 dB means that the drive power is below 160 W, and solid state amplifiers can be used; they will be installed near to the klystrons in the tunnel. The klystrons will be mounted horizontally together with the pulse transformer inside a container. The complete assembly will be transported using the monorail system to its location in the tunnel, and then installed below the walk way. The goal for klystron lifetime is 60,000 h, but a conservative 40,000 h is used for the estimation of the rate of klystron exchange in the linac tunnel.

	Design	Measurement
Operation Frequency	1300 MHz	1300 MHz
RF Pulse Duration	1.5 ms	1.5 ms
Repetition Rate	10 Hz	5 Hz
Cathode Voltage	110 kV	117 kV
Beam Current	130 A	131 A
HV Pulse Duration	1.7 ms	1.7 ms
No. of Beams	7	7
Microperveance	3.5	3.27
No. of Cavities	6	6
Max. RF Peak Power	10 MW	10 MW
RF Average Power	150 kW	75 kW
Efficiency	70%	65%
Gain	48 dB	48.2 dB
Solenoid Power	4 kW	6 kW

Table 3.3.1: *Design and measured parameters of the multibeam klystron (see [31] for details).*

3.3.3 Modulator

3.3.3.1 Overview

The modulator converts AC line voltage to pulsed high voltage in the 120 kV range to be applied to the klystron cathode. The pulse shape must be as rectangular as possible. The flat top ripple should not exceed $\pm 0.5\%$ in order to limit phase and amplitude variations of the klystron RF output. The rise and fall times of the pulse should be as short as possible to maximise the total efficiency. The pulse-to-pulse stability must be better than $\pm 0.5\%$. In case of klystron gun sparking, the energy deposited into the spark must be limited to a maximum of 20 J. These and other requirements are summarised in table 3.3.2.

Various types of modulators meeting these requirements are conceivable; the most promising solution (with respect to cost, ease of design, and reliability) is a bouncer modulator consisting of a DC high voltage power supply, a pulser unit and a pulse transformer [32]. Several modulators of the bouncer type were built and are in use at the TTF. A detailed description of the modulator is given in [33, 34, 35, 36].

A modulator based on the Superconducting Magnetic Energy Storage (SMES) principle as a possible alternative will be tested at TTF. Here a superconducting solenoid is used instead of a capacitor bank for the intermediate energy storage [37].

	Typical	Maximum
Klystron Gun Voltage	115 kV	120 kV
Klystron Gun Current	130 A	140 A
High Voltage Pulse Duration (70% to 70%)	< 1.7 ms	1.7 ms
High Voltage Rise and Fall Time (0 to 99%)	< 0.2 ms	0.2 ms
High Voltage Flat Top (99% to 99%)	1.37 ms	1.5 ms
Pulse Flatness During Flat Top	< $\pm 0.5\%$	$\pm 0.5\%$
Pulse-to-Pulse Voltage fluctuation	< $\pm 0.5\%$	$\pm 0.5\%$
Energy Deposit in Klystron in Case of Gun Spark	< 20 J	20 J
Pulse Repetition Rate for 90% of the Modulators	5 Hz	5 Hz
Pulse Repetition Rate for 10% of the Modulators	10 Hz	10 Hz
Transformer Ratio	1 : 12	
Filament Voltage	9 V	11 V
Filament Current	50 A	60 A

Table 3.3.2: Modulator requirements.

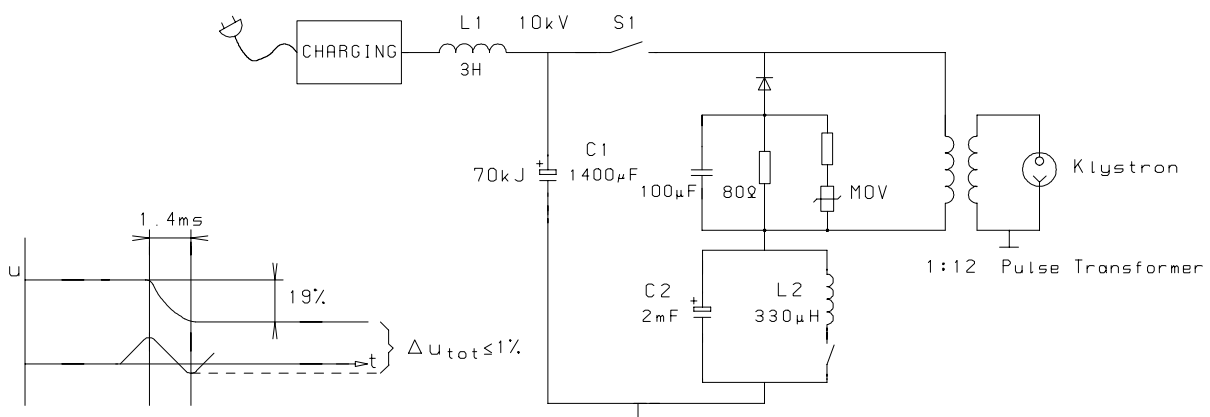


Figure 3.3.3: Modulator circuit (conceptual).

3.3.3.2 Bouncer pulser

The bouncer modulator solution is sketched in figure 3.3.3. During operation the DC power supply keeps capacitor C1 charged to the 10 kV level. The output pulse is started by closing S1, connecting C1 to the pulse transformer primary. Semiconductor devices like Isolated Gate Bipolar Transistors (IGBT) or Integrated Gate-Commutated Thyristors (IGCT) can be used for the switches. The pulse is terminated after 1.57 ms (1.37 ms flat top + ~ 0.2 ms rise time) by opening S1. The nominal current switched by S1 is 1.56 kA. The primary pulse of 10 kV is stepped up by the 1:12 pulse transformer to the klystron operating level (maximum 120 kV).

During the pulse, capacitor C1 discharges by 19% of its initial voltage, putting an intolerable slope on the output pulse. To correct the slope to the 1% level without

resorting to a 29 mF capacitor at the C1 location, a bouncer circuit is used: this is a resonant LC circuit, which creates a single sine wave with a period of 5 ms and an amplitude at the 1 kV level. The bouncer is triggered slightly before the main pulse so that the linear (bipolar) portion of the cycle compensates the slope from C1. The size of the pulser units are 2.8 m (L) \times 1.6 m (W) \times 2.0 m (H), and will be installed in the access halls (typically 100 per hall).

3.3.3.3 Pulse transformer

The output pulse of the pulser unit has a maximum amplitude of 10 kV, and must be transformed to the 120 kV level by means of a pulse transformer. The transformer should not significantly distort the rectangular pulse. The rise time of the high voltage pulse is mainly determined by the transformer's leakage inductance, which must therefore be kept to a minimum. Several transformers with leakage inductances slightly above 300 μ H have been built and operated at TTF. Some new transformers having even less than 200 μ H are now available and will be used at TTF. The voltage level of 120 kV requires the transformer to be installed in a tank filled with transformer oil; the klystron socket housing the cathode will be installed in the same tank.

The pulse transformer tanks have the dimensions 3.2 m (L) \times 1.2 m (W) \times 1.4 m (H), and weigh 6.5 t each. They will be installed below the walk way in the tunnel.

3.3.3.4 Pulse cable

The energy transport from the modulator to the transformer will be done via pulse cables. The maximum distance between the modulators in the service halls and the pulse transformers in the tunnel is \sim 2.8 km. The required cross section of the copper current lead is 300 mm² per conductor. In order to transmit the high voltage pulse without significantly distorting the pulse shape (especially at the leading edge of the pulse), the cable impedance must be matched to the klystron impedance, and the skin effect must be minimized. To achieve this, four coaxial cables will be used, each having a conductor cross section of 75 mm², and an outer diameter of 30 mm. The cable construction is shown in figure 3.3.4. The cable impedance Z_0 of the four cables equals 6.45 Ω . Coaxial cables are used to prevent electromagnetic noise in the tunnel. The inner lead is at high potential (12 kV); the outer lead is at the potential of the bouncer circuit (\pm 2 kV). VPE will be used as insulation material, and an aluminium foil shield and a protective outer coating help to minimise the risk of fire. Additional line matching to the pulse transformer will be done via an RC network. The power losses in the cable will be 2% on average. Simulation results and further information on the cable are given in [38].

The cables will be placed in cable trays welded to steel anchor plates integrated into the tunnel wall. They will be cooled by natural air convection.

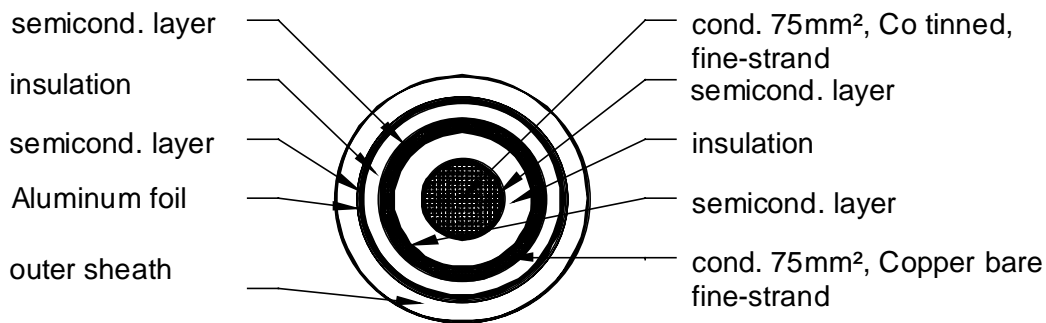


Figure 3.3.4: Construction of the pulse cable.

3.3.3.5 High voltage power supply

The high voltage power supply — which charges the main capacitor of the pulser — has to meet two requirements:

- the capacitor has to be charged to an accurate value of voltage in order to obtain the same voltage at the klystron from pulse to pulse; and
- the low repetition frequency of 5 Hz and 10 Hz respectively has to be suppressed in order not to produce disturbances in the mains.

The amount of allowed disturbance is defined by the German norm VDE 0838 or the equivalent European norm EN 61000. For the 5 Hz and 10 Hz repetition rate of TESLA, the allowed amount of distortion (D) is 0.5% of the short circuit power. TESLA will have a distributed power system with a voltage of 20 kV. In each service hall a maximum of 100 modulators are to be installed having an average real power consumption of up to 15 MW. The service halls have a short circuit power (S_{sc}) of approximately 200 MVA: therefore from $D = \Delta S / S_{sc} \leq 0.5\%$ it follows that the allowed variation of the input power must be $\Delta S \leq 1$ MVA per hall or ≤ 10 kVA per RF station. The corresponding input power variation for a single modulator must be less than 6.5% of its nominal power (changes in reactive power included).

Each modulator will have a separate switch mode power supply. The input will be the standard grid three phase voltage. The voltage output is 12 kV, and the nominal power of each supply is 150 kW at 5 Hz (300 kW at 10 Hz) repetition rate. The power supply is built in modules, ensuring a high reliability. Buck converters will be used as switch mode units; series resonant converters are a possible alternative. The advantages of this solution are:

- the system has a high redundancy — failure of one modulator or power supply leaves the other modulators unaffected;
- failure of one single power supply module still allows the modulator to be operated;

- each power supply can be regulated independently with a high regulation dynamics;
- the low voltage level means the switch gear is available as a low-price commercial off-the-shelf component;
- no additional high-voltage safety requirements are necessary during maintenance or replacement of a power supply.

The power supply is regulated by digital self-learning regulation of the input power, made possible by the high regulation dynamics. In addition, the voltage at the capacitor bank at the trigger time of the pulse will be regulated to within 0.5%.

The size of the high voltage power supply is 1.2 m (L) \times 1.6 m (W) \times 2.0 m (H). Further information about the power supplies can be found in [39].

3.3.3.6 Auxiliary power supplies

In addition to the main high voltage power supplies, operation of the klystron and modulator require additional auxiliary supplies for:

- the klystron focusing solenoid;
- the klystron filament;
- the klystron vacuum pump; and
- the core bias for the pulse transformer.

The auxiliary power supplies will be installed below the walk way in the tunnel.

3.3.4 Power requirements

The klystrons must deliver the maximum RF power of 9.7 MW when required, taking into account the regulation reserve of 10% for phase and amplitude control and 6% for losses in the waveguide distribution. To allow for the regulation, the klystron must be run slightly below saturation, and the efficiency drops from the design (saturation) value of 70% by a few percent. Taking this into account, we assume a klystron efficiency of 65%; a corresponding klystron voltage of 117 kV is then required. The high voltage pulse of the modulator meets the requirement during the flat top but not during the rise and fall times. The pulse rise time is of the order of 200 μ s: however the average rise time of the HV pulse at the klystrons will be greater than 200 μ s because of the long cables between the pulse forming units in the service buildings, and the pulse transformer-klystron units in the tunnel.

Since the first 420 μ s of the RF pulse will only be used to fill the superconducting cavities with power, it can already start during the rise time of the high voltage pulse: the klystron RF output power during the rise time will be lower than that during the flat top, but can still be used to fill the cavities. The RF pulse can be started when the

Peak RF power per RF station	9.7 MW
Duty cycle	0.685%
Average RF power available per RF station	66 kW
Klystron efficiency	65%
Modulator efficiency	85%
Total efficiency	55%
AC power per RF station	120 kW
Auxiliary power per RF station	14 kW
incl. LLRF and waveguide tuner	
Total wall plug power per station	134 kW
Number of active stations	560
Total wall plug power	75 MW

Table 3.3.3: *Efficiencies and power requirements of the RF system.*

klystron voltage reaches 80% of the flat top voltage — about $100\ \mu\text{s}$ after the beginning of the high voltage pulse. The klystron output power at this voltage is about 4 MW. The RF phase shift of $\sim 320^\circ$ in about $200\ \mu\text{s}$ due to the changing klystron voltage can be compensated by the low level RF control system. In this way, the rise time efficiency¹ of the modulator can be increased to 96%. The electronic efficiency of the modulator is 90%. Taking into account the additional ohmic losses of 2% in the pulse cables, this results in a total modulator efficiency of 85%.

In order to generate 9.7 MW in a 1.37 ms long RF pulse at 5 Hz repetition rate, an average primary AC power of 120 kW per RF station is required. In addition, 14 kW for the auxiliary power supplies must be added. The total average AC power required for 560 active RF stations is therefore 75 MW. Table 3.3.3 summarises the power requirements for RF generation in the main linac. An additional 6 MW AC power must be added to these numbers for the FEL operation.

3.3.5 Modulator and klystron protection and control

A comprehensive interlock system is required for the reliable and safe operation of the RF system. In the event of a klystron gun spark, the energy deposited in the spark must be kept below 20 J to avoid damage of the klystron gun. The response to a spark will be an immediate opening of the relevant IG(B)CT switch to disconnect the capacitor bank from the sparking klystron. The energy stored in the transformer leakage inductance and power transmission cable is dissipated in two networks: one at the cable end near the IG(B)CT consisting essentially of a reverse diode and a resistor; the second made up by an $80\ \Omega$ resistor across the transformer primary and by a $100\ \mu\text{F}$ capacitor which limits the peak inverse voltage at the primary to 800 V when the IG(B)CT is opened. In addition a crowbar is fired. Other important interlocks are: cooling water flow and

¹defined as the ratio of the energy per high voltage pulse used for RF generation, to the total energy per high voltage pulse.

temperature; focusing solenoid current; vacuum. Additional interlock conditions result from: sparks in the RF distribution system; reflected power; RF leaks; power couplers; and cryogenics.

In order to meet the different safety requirements, several different interlock techniques will be used. The interlock which inhibits RF operation during tunnel access is accomplished by two separate and independent hard-wired systems, which switch off the klystron RF drive power and the modulators high voltage power supply.

The technical interlock — which protects the linac and the RF station in case of malfunction — will be realized using programmable logic controller (PLC) and system-on-programmable-chip (SOPC) techniques. Both systems are industrial standards, and help is available for planning, structure and programming. In addition hardware for almost all applications can be obtained from several manufactures. Besides system protection and providing start up and shut down procedures for the RF stations, the interlock system will offer comprehensive diagnostics of the RF systems. It will measure and diagnose parameters, and adjust set points within certain limits for each RF station and its subsystems. Communication with the accelerator main control system will be accomplished by a VME bus.

The interlock system will be divided into two units: one installed in an electronic rack in the tunnel near to the klystron, and another installed near to the pulser and the high voltage power supply unit in the access hall. Connection and communication between these two units are accomplished by glass fiber cables, allowing fast transfer of the interlock signals. To reduce the number of interconnecting cables, the interlocks of each unit are summarised into categories, and only these sum interlocks will be exchanged between units. Each unit is connected via its own VME bus to the main control system.

3.3.6 RF waveguide distribution system

Figure 3.3.5 illustrates the RF distribution concept. The 10 MW multibeam klystron has two RF output windows and has to supply 36 9-cell cavities, installed in three modules. The RF distribution is based on two symmetrical systems, each supplying 18 cavities. A linear system branching off identical amounts of power for each cavity from a single line by means of directional couplers will be used; it matches the linear tunnel geometry best and leads to lower waveguide losses than a tree-like distribution system, because long parallel waveguide lines can be avoided. Such a system is already in use for the HERA superconducting RF system and has also been successfully tested at TTF.

Circulators are indispensable: they have to protect the klystron against reflected power at the start and end of the RF pulse, and during the filling time of the cavity. In conjunction with load resistors and the power input coupler, the circulators define the loaded cavity impedance as seen by the beam.

Only 4% of the average power generated by one klystron is lost in the waveguides, with an additional 2% in the circulators. Thermal expansion will result in an RF phase shift of 6° and 12° for operation at full power and pulse duration at 5 Hz and 10 Hz

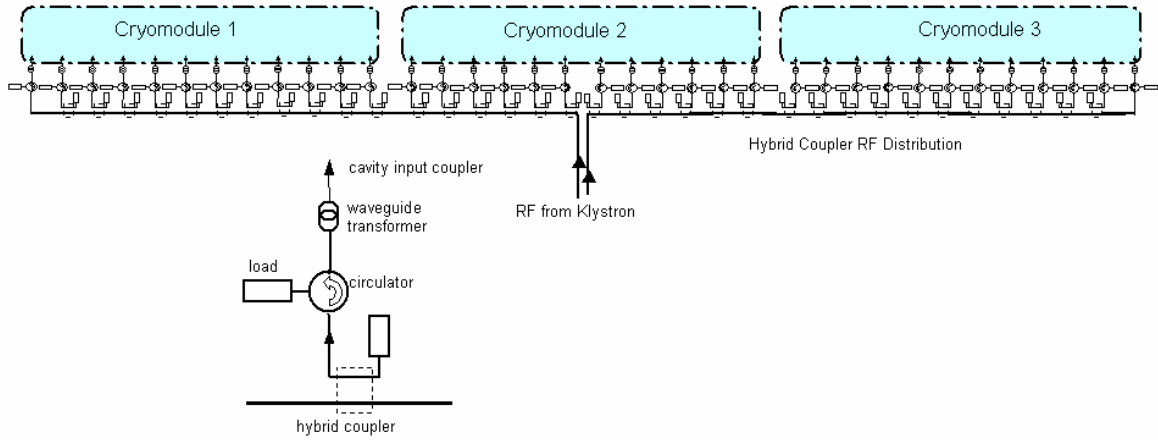


Figure 3.3.5: *RF waveguide distribution of one RF station.*

respectively. The phase shift can be compensated easily by the waveguide transformers (three-stub waveguide transformer) installed between the circulators and each cavity. The waveguide transformers provide an impedance matching range from $1/3 Z_W$ to $3.0 Z_W$ and the possibility of $\pm 50^\circ$ phase adjustment. Each stub is equipped with a motor which is controlled by the low level RF system.

The RF distribution system will be equipped with several interlock sensors, e.g. reflected power, sparking and RF leakage. Similar systems are in use at TTF.

3.3.7 Low level RF

3.3.7.1 Control requirements

The requirements for amplitude and phase stability of the vector-sum of 36 cavities are driven by the maximum tolerable energy spread in the beam. It is desirable to keep the bunch-to-bunch energy spread below the single-bunch energy spread of $5 \cdot 10^{-4}$ in order to assure that the bunch-to-bunch chromatic effects will not be a dominant emittance growth factor. The bunch-to-bunch rms energy error due to *systematic* errors of all the klystrons can be suppressed to the level of $3 \cdot 10^{-4}$: The tolerance for the *uncorrelated* random errors of each individual klystron is set such that the total rms error is not greater than the systematic error. If N_k is the number of klystrons per linac ($N_k = 280$), then the maximum allowed uncorrelated error for each klystron is $\sqrt{N_k} \times 3 \cdot 10^{-4} \approx 5 \cdot 10^{-3}$.

In the following the layout of the RF control system is summarised; more details can be found in refs. [3, 40, 41, 42, 43, 44].

3.3.7.2 RF control design considerations

An important constraint is that the RF power needed for control should be minimized. The RF control system must also be robust against variations of system parameters

such as beam loading and klystron gain, especially close to klystron saturation. The pulsed structure of the RF power and the beam current, which are shown in figure 3.3.6, imposes demanding requirements on the RF control system. Amplitude and phase control is obviously needed during the flat top of $950\ \mu\text{s}$ when the beam is accelerated, but it is equally desirable to control the field during cavity filling to ensure proper beam injection conditions and to minimize the RF power during filling.

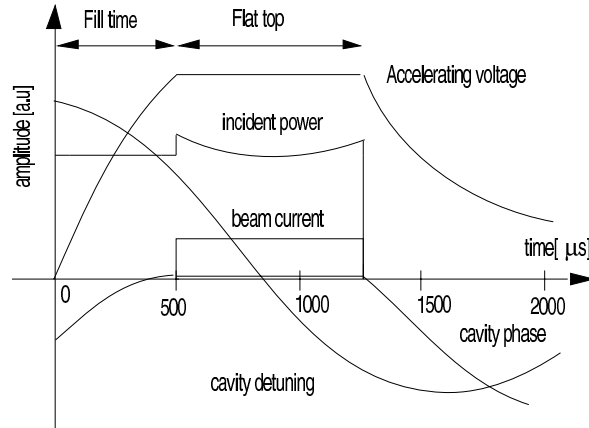


Figure 3.3.6: Various parameters related to the pulsed cavity fields in the superconducting cavities of the TESLA Test Facility.

As a result of Lorentz force detuning and microphonics, the amplitude and phase errors are of the order of 5% and 20 degrees respectively. These errors must be suppressed by a factor of at least 10, and the loop gain must be adequate to meet this goal. Fortunately, the dominant source of errors is repetitive (Lorentz force and beam transients) and can be significantly reduced by the use of feedforward.

3.3.7.3 Design of the TESLA RF control system

Fast amplitude and phase control of the cavity field can only be accomplished by modulating the signal driving the klystron, and hence systematically affects all the associated 36 cavities. A so-called I/Q modulator is used to control both the in-phase (I) and quadrature (Q) components of the cavity field¹. This scheme minimizes coupling between the loops and guarantees control in all four quadrants. The overall scheme of the RF control system is shown in figure 3.3.7.

Digital I/Q detectors are used for the cavity field, incident and reflected waves. The RF signals are converted to an intermediate frequency of 250 kHz and sampled at a rate of 1 MHz (i.e. two consecutive data points describe I and Q of the cavity field). The I and Q component are multiplied by 2×2 rotation matrices to correct the phase offsets

¹I and Q are the two cartesian components of the cavity voltage, from which the amplitude and phase can be readily obtained.

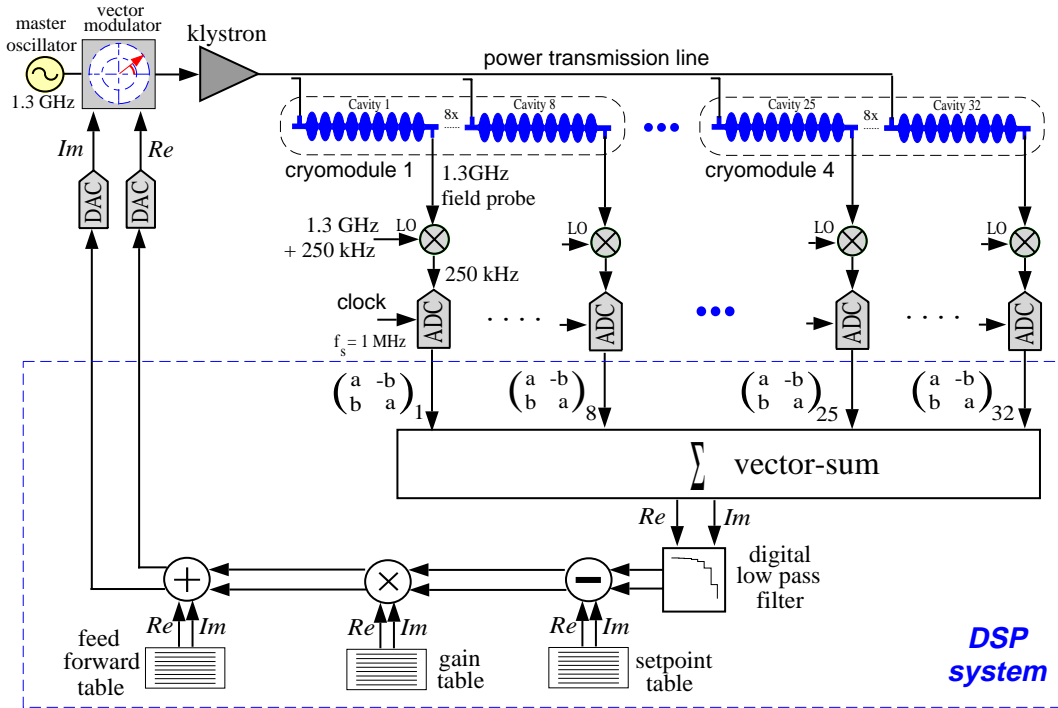


Figure 3.3.7: Schematic of the digital RF feedback system.

and to calibrate the gradients of the individual cavity probe signals. The vector-sum is calculated and corrected for systematic measurement errors. Finally the set point is subtracted and the compensator filter is applied to calculate the new actuator setting (I and Q control inputs to a vector modulator). Feedforward is added from a table in order to minimize the control effort. The feedforward tables are adaptively updated to reflect slowly changing parameters such as average cavity detuning, changes in klystron gain, phase shift in the feedforward path, and general changes in operating parameters. The operation of the more than 560 linac RF systems will be highly automated by the implementation of a finite state machine, which has access to high level applications including the adjustment of the loop phase, vector-sum calibration, frequency and waveguide tuner control, and exception handling.

3.3.7.4 Measured RF control performance at the TTF

The purpose of the TTF is to demonstrate that all major accelerator sub-systems meet the technical and operational requirements of the TESLA linear collider. Currently the TTF linac is operated with one klystron driving 16 cavities. The cavities have been routinely operated at a gradient of 15 MV/m providing a beam energy of 260 MeV. The requirements of $\sigma_A/A < 2 \cdot 10^{-3}$ for amplitude stability and of $\sigma_\Phi < 0.5^\circ$ phase stability have been achieved with feedback only, the stability being verified by beam measurements. The residual fluctuations are dominated by a repetitive component which is further reduced using the adaptive feedforward by about one order of magni-

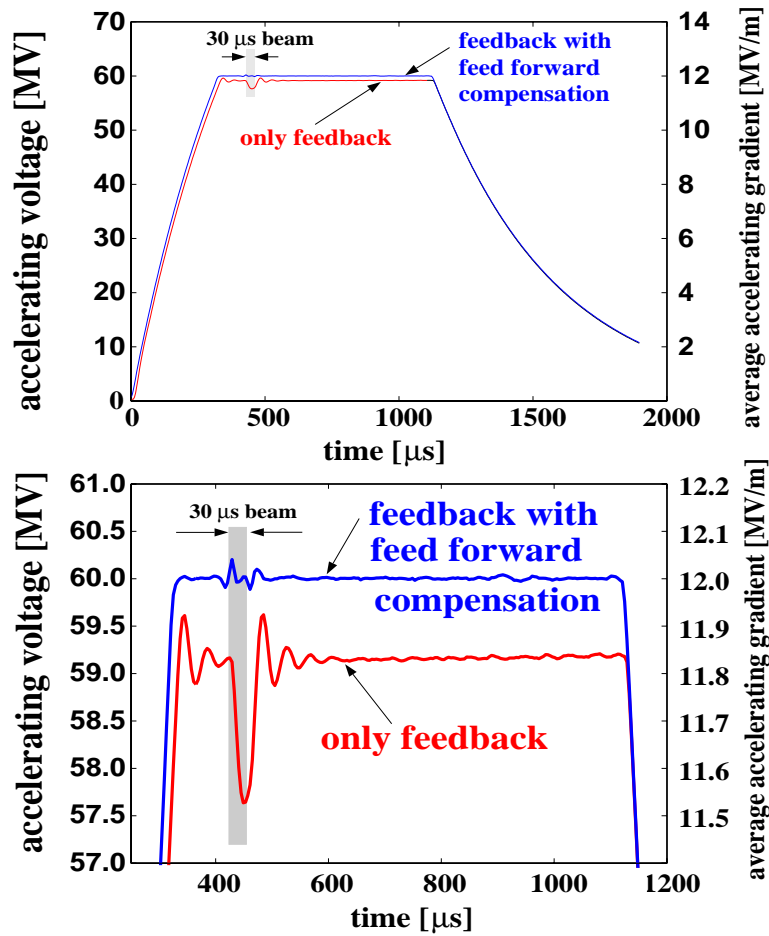


Figure 3.3.8: *Field stability with and without adaptive feed forward.*

tude, thereby exceeding the design goals significantly. The high degree of field stability achieved is mainly due to the low microphonic noise levels. A typical result of measured field stability with and without the adaptive feedforward is shown in figure 3.3.8.

3.3.8 RF components test hall

During the installation of the RF system for the linac, all incoming RF components will be received, inspected, tested and prepared for installation in a components test hall. After installation is complete, the hall will be used for maintenance work and storage of spare components required during linac operation. In addition, the hall will still continue to be used to receive klystrons delivered by industry at a rate of about ten per month. The additional investment for the test hall is included in the total RF system cost estimate.

Bibliography

- [1] V. Balakin, A. Novokhatski, V. Smirnov, *VLEPP: Transverse Beam Dynamics*, Proc. 12th Int. Conf. on High Energy Accelerators, Fermilab 1983, p. 119.
- [2] V. Tsakanov, *Beam Dynamics Study for TESLA with the Integrated FEL*, DESY TESLA-99-21, 1999.
- [3] R. Brinkmann, G. Materlik, J. Roßbach and A. Wagner (eds.), *Conceptual Design of a 500 GeV e+e- Linear Collider with Integrated X-ray Laser Facility*, DESY-97-048 and ECFA-97-182, 1997, chapter 3.
- [4] A. Mosnier, *Longitudinal and Transverse Wakes for the TESLA Cavity*, DESY TESLA-93-11, 1993.
- [5] A. Novokhatski, M. Timm and T. Weiland, *Single Bunch Energy Spread in the TESLA Cryomodule*, DESY TESLA-99-16, 1999.
- [6] A. Novokhatski, M. Timm and T. Weiland, *Transition Dynamics of the Wake Fields of Ultra Short Bunches*, DESY TESLA-00-03, 2000.
- [7] C. E. Adolphsen et al., *Beam Based Alignment Technique for the SLC Linac*, SLAC-PUB-4902, 1989.
- [8] R. Assmann, T. Chen, F. J. Decker, M. Minty, T. Raubenheimer and R. Siemann, *Quadrupole Alignment and Trajectory Correction for Future Linear Colliders: SLC Tests of a Dispersion-Free Steering Algorithm*, Proc. Int. Workshop on Accelerator Alignment, Tsukuba 1996, KEK-95-12, p. 463.
- [9] P. Tenenbaum et al., *Beam-Based Alignment of the Final Focus Test Beam*, SLAC-PUB-7058, 1995.
- [10] M. Böge et al., *Application of a Beam Based Alignment Technique for Optimizing the Electron Spin Polarization at HERA*, Proc. 5th EPAC, Sitges 1996, Vol. I, p. 439.
- [11] R. Assmann, P. Raimondi, G. Roy and J. Wenninger, *A Method for Simultaneous Optimisation of Orbit and Dispersion in Storage Rings*, Proc. 7th EPAC, Vienna 2000, p. 1462.
- [12] T. Raubenheimer and R. D. Ruth, *A Dispersion Free Trajectory Correction Technique for Linear Colliders*, Nucl. Instr. Meth. A **302** (1991) 191.
- [13] C. Magne and M. Wendt, *Beam Position Monitors for the TESLA Accelerator Complex*, DESY TESLA-00-41, 2000.
- [14] G. A. Amatuni, V. G. Khachatryan, V. Tsakanov and R. Brinkmann, *On the Single Bunch Emittance Preservation in TESLA*, DESY TESLA-01-02, 2001.

-
- [15] S. Fartoukh et al., *Evidence for a Strongly Coupled Dipole Mode with Insufficient Damping in the TTF First Accelerating Module*, Proc. Particle Accelerator Conf., New York 1999, p. 922.
- [16] N. Baboi, M. Dohlus, H.-W. Glock, C. Magne, A. Mosnier and O. Napoly, *Investigation of a High-Q Dipole Mode at the TESLA Cavities*, Proc. 7th EPAC, Vienna 2000, p. 1107.
- [17] N. Baboi and R. Brinkmann, *Higher Order Mode Effects and Multi-Bunch Orbit Stability in the TESLA Main Linac*, DESY TESLA-00-28, 2000.
- [18] R. Brinkmann and J. Roßbach, *Observation of Orbit Motion in HERA Covering Eight Decades in Frequency*, Nucl. Instr. Meth. **A 350** (1994) 8.
- [19] V. Shiltsev, B. Baklakov and P. Lebedev, *Measurements of Ground Vibrations and Orbit Motion in HERA*, DESY HERA-95-06, 1995.
- [20] J. G. Weisend II, R. Bandelmann, D. Barni, M. Bonezzi, G. Grygiel, R. Lange, C. Pagani, B. Petersen, P. Pierini, D. Sellmann, S. Wolff, *The TESLA Test Facility (TTF) Cryomodule: A Summary of Work to Date*, Proc. CEC/ICMC 1999, Montreal 1999, published in Advances in Cryogenic Engineering **45A** (2000) 825.
- [21] C. Pagani, D. Barni, M. Bonezzi, J. G. Weisend II, *Further Improvements of the TESLA Test Facility (TTF) Cryostat in View of the TESLA Collider*, Proc. CEC/ICMC 1999, Montreal 1999, published in Advances in Cryogenic Engineering **45A** (2000) 939.
- [22] M. Liepe, W.D. Moeller, S.N. Simrock, *Dynamic Lorentz Force Compensation with a Fast Piezoelectric Tuner*, DESY TESLA-01-03, 2001.
- [23] M. Dohlus, H.P. Wedekind and K. Zapfe, *Wakefield Induced Losses in the Manual Valves of the TESLA Cryomodule*, DESY TESLA-00-39, 2000.
- [24] R. Brinkmann, M. Dohlus, D. Trines, A. Novokhatski, M. Timm, T. Weiland, P. Huelsmann, C. Rieck, K. Scharnberg, P. Schmueser, *THz Wakefields and Their Effect on the Superconducting Cavities in TESLA*, Proc. 7th EPAC, Vienna 2000, p. 2028.
- [25] A. Joestingmeier, M. Dohlus, C. Cramer, *Photon Diffusion Model for TTF2*, DESY TESLA-00-11, 2000.
- [26] A. Joestingmeier, M. Dohlus, M. Wendt, C. Cramer, *Theoretical and Practical Investigations Concerning the Design of a HOM Broadband Absorber for TESLA*, DESY TESLA-00-10, 2000.
- [27] B. Mikijeli, I. Campisi, *Development of an Artificial Dielectric Ceramic for the use at CEBAF*, Proceedings of the Workshop on Microwave-Absorbing Materials for Accelerators, CEBAF, 1993.

-
- [28] C. Bearzatto, M. Bres, G. Faillon, *Advantages of Multiple Beam Klystrons*, ITG Garmisch-Partenkirchen, May 4 to 5, 1992.
- [29] R. Palmer, *Introduction to Cluster Klystrons*, Proceedings of the International Workshop on Pulsed RF Power Sources For Linear Colliders, RF93, Protvino, July 1993, p. 28.
- [30] A. Beunas, G. Faillon, *10 MW/1.5 ms, L-band Multi-beam Klystron*, Proc. Conf. Displays and Vacuum Electronics, Garmisch-Partenkirchen, Germany, April 29-30 1998.
- [31] [A. Beunas](#), [G. Faillon](#), [S. Choroba](#), [A. Gamp](#), *A High Efficiency Long Pulse Multi Beam Klystron for the TESLA Linear Collider*, DESY TESLA-01-01, 2001.
- [32] [W. Bothe](#), *Pulse Generation for TESLA, a Comparison of Various Methods*, DESY TESLA-94-21, 1994.
- [33] [H. Pfeffer](#), [C. Jensen](#), [S. Hays](#), [L. Bartelson](#), *The TESLA Modulator*, DESY TESLA-93-30, 1993.
- [34] [D. A. Edwards \(ed.\)](#), *The TESLA Test Facility LINAC-Design Report*, DESY TESLA-95-01, 1995.
- [35] [H. Pfeffer](#), [L. Bartelson](#), [K. Bourkland](#), [C. Jensen](#), [Q. Kerns](#), [P. Prieto](#), [G. Saewert](#), [D. Wolff](#), *A Long Pulse Modulator for Reduced Size and Cost*, presented at the 21st Int. Power Modulator Symposium, Costa Mesa, CA, June 1994.
- [36] [H. Pfeffer](#), [L. Bartelson](#), [K. Bourkland](#), [C. Jensen](#), [P. Prieto](#), [G. Saewert](#), [D. Wolff](#), *A Second Long Pulse Modulator For TESLA Using IGBTs*, Proc. 5th EPAC, Sitges 1996, p. 2585.
- [37] [K.P. Juengst](#), [G. Kuperman](#), [R. Gehring](#), *SMES Based Power Modulator - Status Dec. 2000*, Reports of Forschungszentrum Karlsruhe, FZKA 6568, Jan. 2001.
- [38] [H.-J. Eckoldt](#), *Pulse Cables for TESLA*, DESY TESLA-00-35, 2000.
- [39] [H.-J. Eckoldt](#), [N. Heidbrook](#), *Constant Power Power Supplies for the TESLA Modulator*, DESY TESLA-00-36, 2000.
- [40] [M. Liepe](#), [S. N. Simrock](#), *Adaptive Feed Forward for Digital RF Control System at the TESLA Test Facility*, Proc. 6th EPAC, Stockholm 1998, p. 1735.
- [41] [M. Hüning](#), [S. N. Simrock](#), *System Identification for the Digital RF Control at the TESLA Test Facility*, Proc. 6th EPAC, Stockholm 1998, p. 1732.
- [42] [S. N. Simrock](#), [I. Altmann](#), [K. Rehlich](#), [T. Schilcher](#), *Design of the Digital RF Control System for the TESLA Test Facility*, Proc. 5th EPAC, Sitges 1996, p. 349.

- [43] [S. N. Simrock](#), [T. Schilcher](#), *Transient Beam Loading based Calibration of the Vector-Sum for the TESLA Test Facility*, Proc. 5th EPAC, Sitges 1996, p. 1866.
- [44] [B. Aune et al.](#), *Superconducting TESLA Cavities*, Published in Phys.Rev.ST Accel.Beams 3:092001, 2000.